Geology, geochronology and fluid characteristics of the Pingqiu gold deposit, Southeastern Guizhou Province, China

An-Lu Liu [a,b], Xiao-Jun Zhang [a,b,*], Thomas Ulrich [c], Jun Zhang [a,b], Man-Rong Jiang [a,b], Wen-Hao Liu [a,b]

[a] Faculty of Earth Resources, China University of Geosciences, Wuhan, Hubei Province 430074, China
[b] National Demonstration Center for Experimental Mineral Exploration Education, China University of Geosciences, Wuhan, Hubei Province 430074, China
[c] Department of Geoscience, Aarhus University, Høegh-Guldbergs Gade 2, DK-8000 Aarhus C, Denmark

A R T I C L E I N F O

A B S T R A C T

The junction of the southeastern Guizhou, the southwestern Hunan, and the northern Guangxi regions is located within the southwestern Jiangnan orogen and forms a NE-trending $\sim$250 km gold belt containing more than 100 gold deposits and occurrences. The Pingqiu gold deposit is one of the numerous lode gold deposits in the southeastern Guizhou district. Gold mineralization is hosted in Neoproterozoic lower greenschist facies metamorphic rocks and controlled by fold-related structures. Vein types present at Pingqiu include bedding-parallel and discordant types, with saddle-reefs and their down limb extensions dominating but with lesser discordant types. The major sulfide minerals are arsenopyrite and pyrite, with minor sphalerite, galena, chalcopyrite, and rare pyrrhotite, marcasite, and tetrahedrite. Much of the gold is μm- to mm-sized grains, and occurs as fracture-controlled isolated grains or filaments in quartz, galena, sphalerite, pyrite, and wallrock.

Three types of fluid inclusions are distinguished in hydrothermal minerals. Type 1 aqueous inclusions have homogenization temperatures of 171–396 °C and salinities of 1.4–9.8 wt% NaCl equiv. Type 2 aqueous-carbonic inclusions yield final homogenization temperatures of 187–350 °C, with salinities of 0.2–7.7 wt% NaCl equiv. Type 3 inclusions are carbonic inclusions with variable relative content of CO_2 and CH_4, and minor amounts of N_2 and H_2O. The close association of CO_2-rich inclusions and H_2O-rich inclusions in groups and along the same trail suggests the presence of fluid immiscibility. The calculated $\delta^{18}O_{H2O}$ values range from 4.3‰ to 8.3‰ and δD_{H2O} values of fluid inclusions vary from −55.8‰ to −46.9‰. A metamorphic origin is preferred on the basis of geological background and analogies with other similar deposit types.

Two ore-related sericite samples yield well-defined $^{40}Ar/^{39}Ar$ plateau ages of 425.7 ± 1.7 Ma and 425.2 ± 1.3 Ma, respectively. These data overlap the duration of the Caledonian gold mineralization along the Jiangnan orogen, and suggest that gold mineralization was post-peak regional metamorphism and occurred during the later stages of the Caledonian orogeny.

Overall, the Pingqiu gold deposit displays many of the principal characteristics of the Bendigo gold mines in the western Lachlan Orogen (SE Australia) and the Dufferin gold deposit in the Meguma Terrane (Nova Scotia, Canada) but also some important differences, which may lead to the disparity in gold endowment. However, the structural make-up at deposit scale, and the shallow mining depth at present indicate that the Pingqiu gold deposit may have considerable gold potential at depth.

1. Introduction

The southeastern Guizhou district lies at the southwestern end of the Jiangnan orogen and was one of the most important gold producers in China during the 20th century. Two types of mineral-ization, gold-bearing quartz veins and alluvial deposits, were exploited from the 11th century (Wang et al., 2006). A proliferation of exploration activity from the 1970s to today resulted in the discovery and mining of nearly 50 small to medium sized low-sulfide gold deposits (Wang et al., 2006). Reported total gold production was 20 tonnes during the period from 1990 through 2000, and particularly annual gold production was 6 tonnes in 1997 (Ran and Li, 2007), but figures on total production between 2000 and 2010 are not available. Mining has occurred at a few locations since 2010,

* Corresponding author at: Faculty of Earth Resources, China University of Geosciences, Wuhan, Hubei Province 430074, China.
E-mail address: xjzhang01@cug.edu.cn (X.-J. Zhang).

and the production increased gradually from less than 1 tonne in 2013 to 3.5 tonnes in 2015 (Wu, 2013, 2014, 2015). Taken together, available records indicate that the district has produced 30–50 tonnes (1.06–1.76 Moz) Au. However, no actual production figures from single deposits have been published.

Gold mineralization occurs throughout the Neoproterozoic Xiajiang Group and mainly consists of bedding-concordant and -discordant veins within or near the hinges of regional-scale anticlines. The quartz lodes are dominated by quartz, Fe sulfide minerals, and Ca-Mg-Fe-Mn carbonate minerals. Overall, the similar setting, paragenesis of vein minerals, fluid chemistry, and wallrock alteration developed across the whole gold district suggest a similar setting and ore genesis for these deposits. Furthermore, these turbidite-hosted gold deposits are similar in some aspects to those within the western Lachlan Belt in Victoria (SE Australia) (Ramsay et al., 1998; Cox et al., 1991; Bierlein et al., 2004b; Phillips et al., 2012; Lisitsin and Pitcairn, 2016), and the Meguma Terrane (Nova Scotia, Canada) (Kontak et al., 1990; Ryan and Smith, 1998; Lu et al., 2008; Kretschmar and McBride, 2015). Although this district has been studied (Yu, 1997; Lu et al., 2005, 2006; Zhu et al., 2006; Wang et al., 2014; Liu et al., 2014; He et al., 2015; Wu et al., 2015), the origin of the ore-forming fluids is still controversial. He-Ar isotopes extracted from arsenopyrite yielded R/Ra values of between 0.0345 and 0.0776, and $^{4}He/^{40}Ar$ values of between 4.4148 and 7.7154, suggesting a metamorphic origin from the Fanzhao Formation (He et al., 2015). On the other hand, Lu et al. (2006) and Wu et al. (2015), based on H-O isotopes, proposed a magmatic fluid origin. Moreover, few reliable age data have been obtained from these deposits thus far. There have been two previous attempts to directly date gold mineralization in the southeastern Guizhou gold district. Zhu et al. (2006) conducted Rb-Sr dating on fluid inclusions in auriferous quartz from the Pingqiu, Jintou, Tonggu and Jinjing deposits, and bracketed the gold mineralization at between 492 Ma and 340 Ma. Wang et al. (2011) reported Re-Os isochron ages of 400 ± 24 Ma for arsenopyrite in alteration zones from the Pingqiu gold deposit, and 174 ± 15 Ma for arsenopyrite in auriferous quartz veins from the Jinjing gold deposit. Given the intrinsic limitation of Rb-Sr dating on fluid inclusions, and the apparent age discrepancy between different methods applied on the same deposit (e.g. the Jinjing gold deposit), the geological significance of these ages is questionable. Consequently, the ore forming fluids and the timing of gold mineralization need to be further constrained.

The Pingqiu gold deposit is representative of other deposits in the southeastern Guizhou district. It has been mined intermittently for about 200 years (Wang et al., 2006) and is now at an advanced stage of exploration. This offers an opportunity to undertake research that will provide new knowledge of the origin and geochronology of the southeastern Guizhou district. In this paper, we undertake a detailed ore petrology and microscopy study to define the mineral paragenetic sequence and ore-forming stages, we report high-resolution $^{40}Ar/^{39}Ar$ dating on sericite, and we combine Laser Raman, bulk inclusion analyses, microthermometry, and stable isotope analyses of auriferous quartz veins from the Pingqiu gold deposit. The data allow us to better constrain the timing of gold mineralization, the characteristics and origin of the ore-forming fluids, and to compare the characteristics of the veins with those of turbidite-hosted gold deposits elsewhere. The results have implications for the genetic model of the Pingqiu gold deposit and may provide useful guides for further exploration.

2. Regional geology

The junction of the southeastern Guizhou district, the southwestern Hunan province, and the northern Guangxi region is located at the southwestern end of the Jiangnan orogen (Fig. 1A), and forms a NE-trending ~250 km gold belt (Fig. 1B; Zhu et al., 2006; Song, 2014). These are not exclusively gold-only deposits, but Au-Sb-W deposits also occur in the southwestern Hunan province, including the Woxi deposit. Mesoproterozoic to Neoproterozoic turbidites are the principal host rocks in this gold belt (Fig. 1B); they appear to represent continental marginal shelf, slope, and basinal facies deposition (Bureau of Geology and Mineral Resources of Guizhou Province (BGMRGZP), 1987). The southeastern Guizhou district is predominantly underlain by the Neoproterozoic Xiajiang Group, an ~8000 m turbidite sequence that is composed of thickly-bedded sandy-slate, volcanic tuffaceous slate, and a few marble units. The turbiditic sequence displays characteristic Bouma features and has been described in detail by Chen et al. (2006). From base to top, the Xiajiang Group includes the Jialu, Wuye, Fanzhao, Qingshuijiang, Pinglue, and Longli Formations. U-Pb LA-ICPMS dating of detrital zircons from these formations constrain the sedimentation age of the Xiajiang Group to around 815–717 Ma (Gao et al., 2010, 2014; Qin et al., 2015; Ma et al., 2016), reflecting active magmatism along the western Jiangnan orogen that provided abundant detritus to the Neoproterozoic sedimentary sequences (Ma et al., 2016, and references therein).

Several periods of deformation have overprinted the Mesoproterozoic and Neoproterozoic rocks, with regional compression in the Late Mesoproterozoic (D1), Early Paleozoic (D2), Late Paleozoic to Early Cretaceous (D3), and Neogene (D4). The D1 event has shaped the major NE structural trend in this area. The D2 event has had a major influence, resulting in a series of NE-trending folds, faults and cleavages, and gold mineralization. The subsequent D3 event is associated with some NNE-trending folds and NE−NNE-, NW- and EW-trending faults and cleavages. These D3 features appear to post-date gold mineralization and may constitute several generations of development. The D4 event strengthens the regional NE−NNE-trending geometry pattern and is associated with sinistral shearing (BGMRGZP, 1987; Lu et al., 2005; Dai et al., 2010). The structural architecture across the district in defined by the NE-trending folds and faults (Fig. 2). Regional-scale folds occur as upright, gentle to open, and NE- and NNE-trending folds, which can extend to 100 km or more and have a width of typically around 3 to 10 km. The folds are cut by NW- and SE-dipping sinistral strike-slip faults, which strike approximately parallel to fold axial traces and extend over tens of kilometers. These faults can be classified as NE−NNE-, NW-, and EW-trending.

Rocks of the Xiajiang Group have experienced lower greenschist facies metamorphism during orogenic deformation. Detailed analysis using b_0 cell parameter and illite crystalline (IC) of sericite gave an average b_0 value of 0.8995, indicating low pressure, illite-sericite subfacies conditions (BGMRGZP, 2012). Widespread granites and diabases have been observed to the south, north and west of the southeastern Guizhou district, they intruded the base of the Xiajiang Group and yield formation ages of 780–825 Ma (Zeng et al., 2005; Fan et al., 2010; Wang et al., 2012; Chen et al., 2014). To date, no granitic intrusions have been identified in exposures adjacent to the gold deposits in the southeastern Guizhou district, but previous aeromagnetic surveys and remote sensing studies inferred several buried granitic intrusions as well as ultrabasic rocks that deeply underlie several gold deposits, including the Pingqiu gold deposit (Zhu, 1992; Lu et al., 2005; Wang and Tao, 2012).

Primary gold mineralization in the southeastern Guizhou district is largely confined to hinge zones of regional folds generated during the D2 deformation (Fig. 2). Tao et al. (2012) recognized six goldfields in this district, which are parallel to the regional fold and fault trend, according to their ore-controlling structures. Two main types of quartz veins are well recognized throughout the
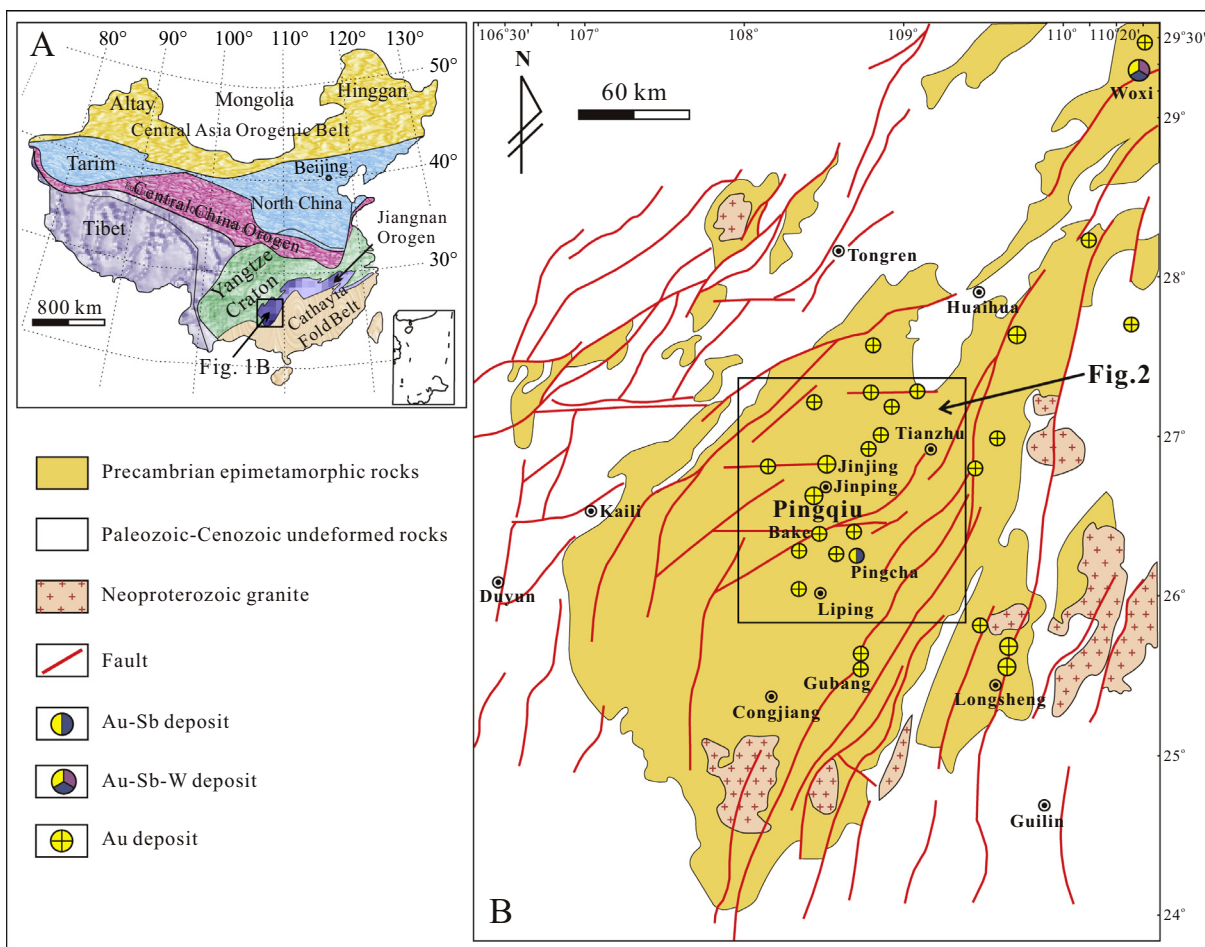
Fig. 1. A. Tectonic framework of mainland China, showing the location of the Jiangnan orogen (modified after Li and Pirajno, 2017; Wang et al., 2014); B. Simplified geological map of the junction of the northern Guangxi, the southeastern Guizhou and the southwestern Hunan, showing the distribution of Precambrian rocks, granitic intrusions and gold deposits (modified after Tao et al., 2009). Note that Carboniferous to Permian sediments are omitted due to the scale (see Fig. 2).

whole district: shear zone-hosted fault veins and anticline-hosted veins. Fault veins are individual quartz laminae (<1–10 cm) and have moderate to steep dips. They form en-echelon-like patterns in the shear zones and intersect the anticline-hosted veins. Most anticline-hosted veins occupy structures related to flexural folding: bedding-parallel, and hinge zone dilation. These veins include saddle-reef veins, generally defining thickened stratabound veins in the fold hinge zone, and leg-reefs which represent the down-limb extensions of saddle-reef veins (Horne and Jodrey, 2001). In addition, there are numerous discordant veins, most of which are interpreted to be related to saddle- and leg-reefs. Most of the historical gold production came from anticline-hosted bedding-concordant veins.

3. Ore deposit geology

The Pingqiu gold deposit consists of several tens of anticline-hosted, gold-bearing quartz veins that can be divided into eight groups (the Mianhuaxi, Jinchangxi, Bize, Shierpan, Chongge, Wuxiangdong, Wucaoxi and Guiweixi) on the basis of their location. Of particular relevance to this work are the Jinchangxi-Shierpan groups (Fig. 3), which are active at present and being mined by small-scale underground operations. Quartz veins lie within the Fanzhao Formation, a tuffaceous metasandstone- and metasiltstone-rich unit of the Xiajiang Group (Lu et al., 2006). The structural style is typical of much of the southeastern Guizhou

gold district, and has been described in detail by Lu et al. (2006). Major anticlines are the NE-trending Daiou, Jinchangxi, and Taozi'ao anticlines (Fig. 4). The Taozi'ao anticline has an asymmetric shape and extends along strike for more than 7 km, with a more steeply dipping (35–80°) northwestern limb and a gently dipping southeastern limb (20–40°). The Daiou anticline has a length of 2.5 km, and also shows an asymmetric shape similar to that of the Taozi'ao anticline. The Jinchangxi anticline has a length of 2.5 km, and at its northwestern termination, it coalesces with the Taozi'ao anticline. Unlike the other two anticlines, the Jinchangxi anticline has a more steeply dipping (30–65°) southeast limb whereas the northwest limb is more gentle (15–35°). The anticlines are cut by a number of NE-trending reverse faults, including the F1 and F2 faults. The F1 fault has a displacement in excess of 90 m and persists along strike for ca. 1800 m. The associated deformation zone has a width of 1–5 m. The upper splay is steep (dip ∼85°), whereas the lower splay is moderately dipping (∼40°). The moderately SE-dipping (45–55°) F2 fault is a reverse fault that extends for a strike length of up to 800 m in the southeastern part of the mine area. It has a width of 1–5 m and displacement of 2–20 m.

Auriferous quartz veins occur in parallel groups on the limbs and at the crests of anticlines within the Fanzhao Formation, especially the second member (Fig. 4). Individual veins have asymmetric shapes with respect to the anticlines (Fig. 5). Seven economic auriferous quartz veins (M6 to M12) have been recognized over a vertical interval of 200 m (from 730 m to 520 m level), however
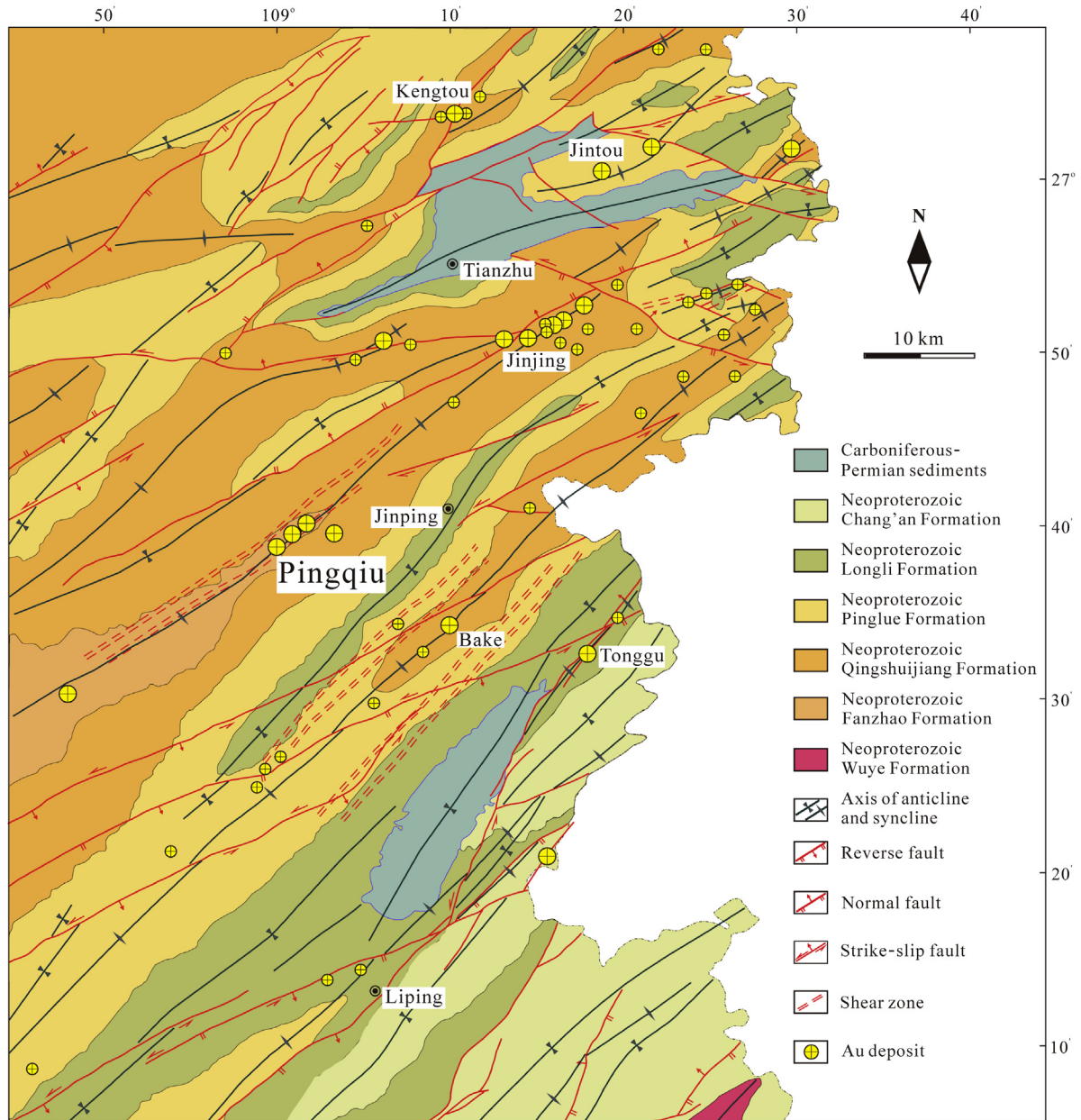
Fig. 2. Geological map of the southeastern Guizhou district (modified after Tao et al., 2013), showing the intimate spatial relationship between large-scale regional folds and gold deposits.
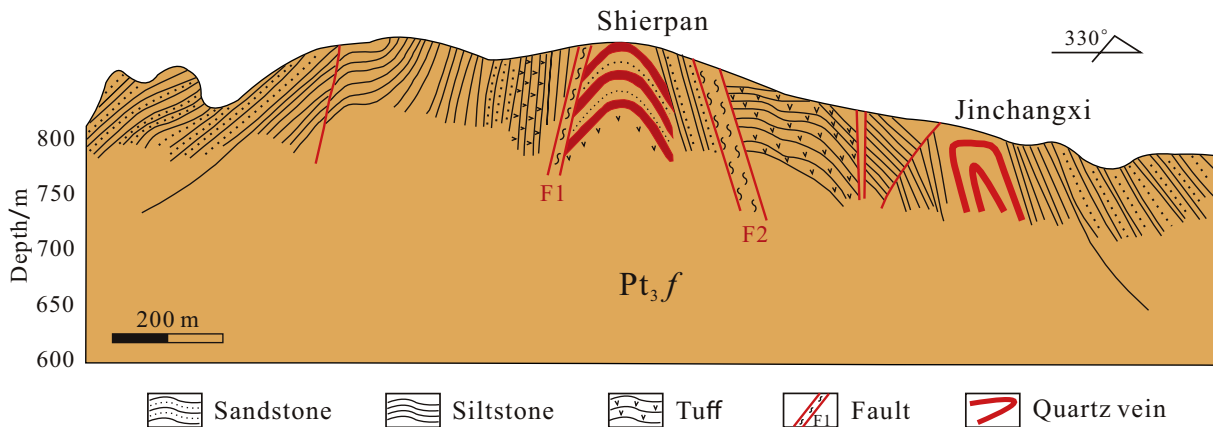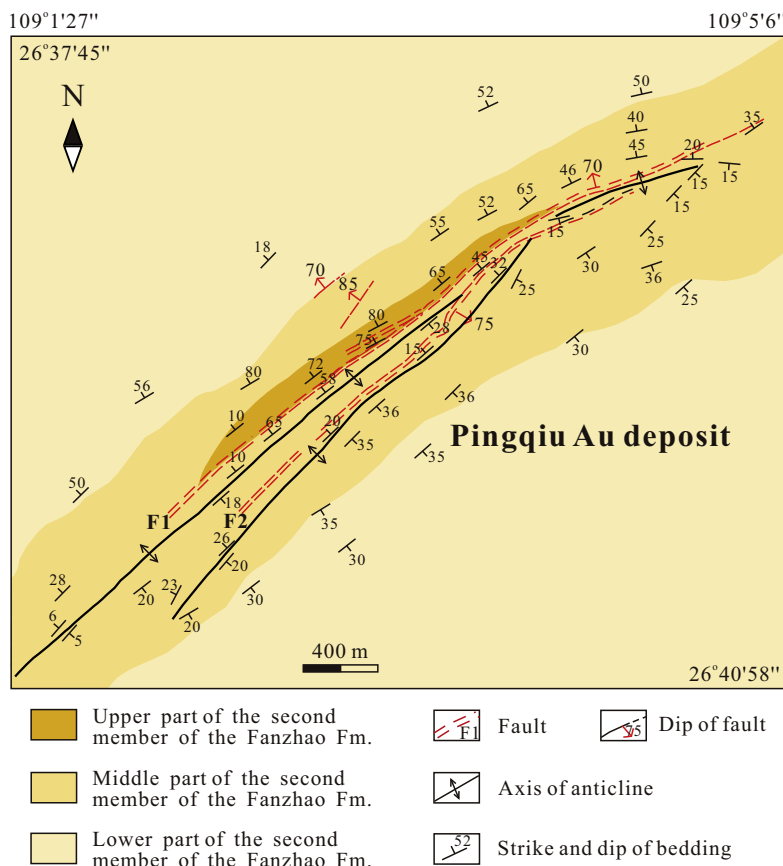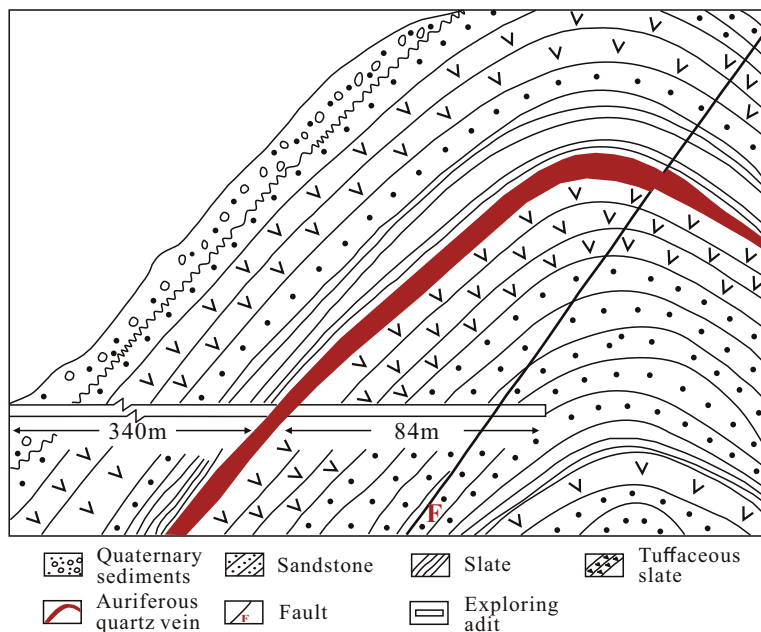

Fig. 3. Cross section showing the distribution and morphology of quartz veins in the Pingqiu gold deposit (modified after Lu et al., 2006).

Fig. 4. Simplified geological map of the Pingqiu gold deposit (modified after No.6 team of Non-ferrous Metals and Nuclear Industry Geological Exploration Bureau of Guizhou, 2002). *Fm.* Formation.

Fig. 5. Cross section of the No. 98 Au orebody, showing its relationship with the controlling anticline (modified after Lu et al., 2006).

the exact number of veins at depth remains to be determined. Both bedding-concordant and -discordant veins occur. Veins on the limbs are mainly bedding-parallel; these veins are several centimeters to 1 m wide and locally buckled (Fig. 6A, B), and extend tens of meters down-dip on each limb. Veins on the limbs are generally continuous, though commonly cut by minor, later faults with small displacement (Fig. 6C). Thin wallrock laminae (Fig. 6C) and wallrock inclusions (Fig. 6B) are widely developed due to repeated
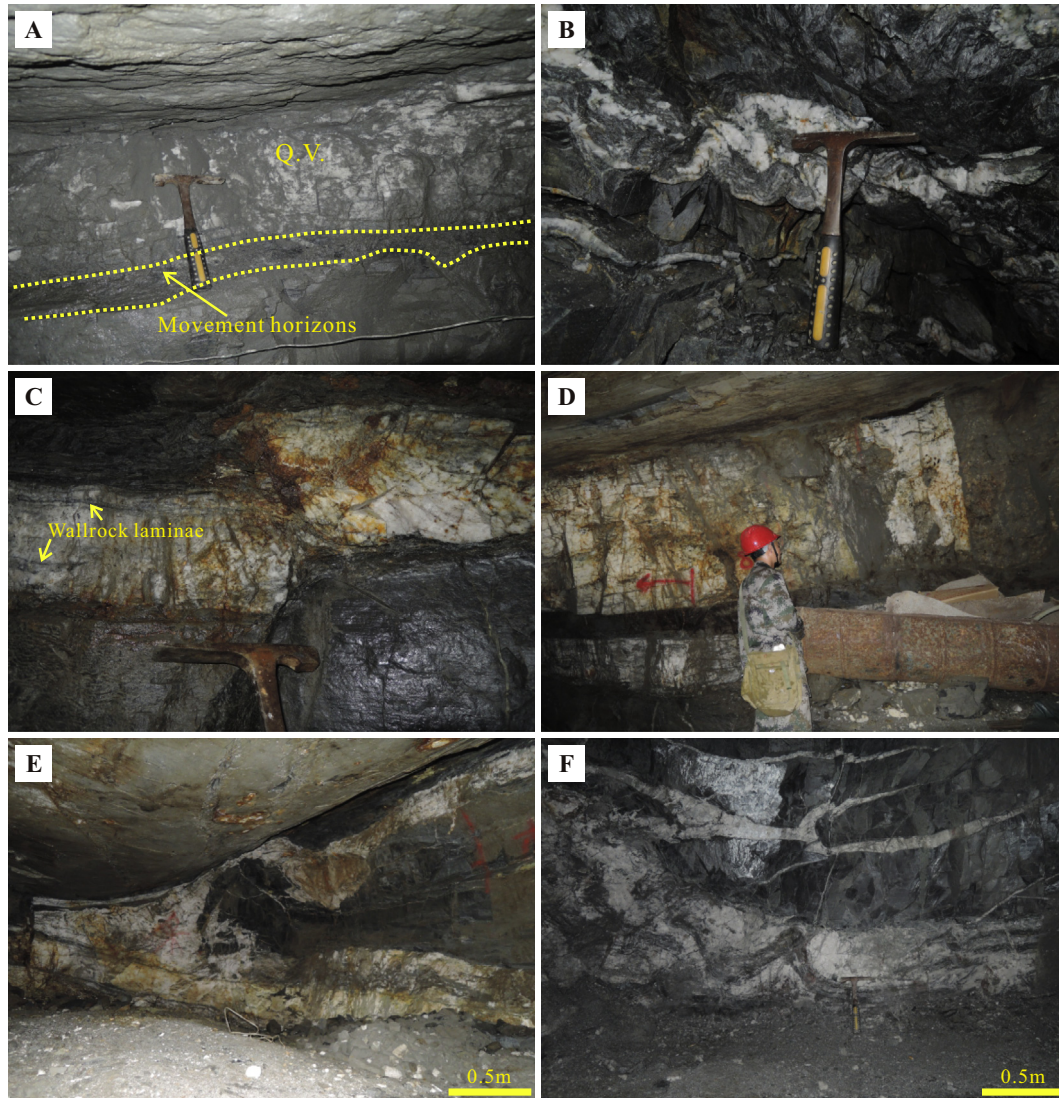
Fig. 6. Photographs showing quartz vein morphology. A. Bedding-parallel vein on the southeast limb, with ~10 cm-thick fault gouge underneath. B. Buckled bedding-parallel vein on the northwest limb. C. Bedding-parallel vein cut by a later fault with small displacement, with wallrock laminae inside. D. Thickened massive quartz vein at the crest of anticline. E. Thickened quartz vein on the northwest limb close to the hinge zone, with crack-seal texture. F. Extensional veins occur immediately adjacent to saddle-reef. *Q. V.* quartz vein.

hydraulic fracturing during vein formation. Saddle-reefs occur at dilatational sites in the hinges of anticlines and are considerably thickened with crescent shapes (over 5 m) (Fig. 6D–F). Abundant ribbon and crack-seal textures can be observed at the hinge zones (Fig. 6E). Bedding-discordant veins are extension veins (Fig. 6F) and mainly found adjacent to the saddle-reefs, but are not restricted to these areas. Movement horizons occurring immediately adjacent to quartz veins on the limbs are defined by 1–10 cm thick zones of fault gouge with angular quartz clasts (Fig. 6A). Here we describe three representative veins.

The M7 vein has a general 050−080° strike, and can be followed along strike for about 350 m, and extends to a vertical depth of more than 80 m. It is an asymmetric structure that varies from 42° to 67° in the southeast, and 35° to 50° in the northwest. The vein varies in thickness from >2 m in the hinge zone to about 10 cm thick on each limb. The M8 vein is over 5 m thick at the crest of the Taozi'ao anticline and extends to over 100 m down-dip on each limb. The southeast limb is moderately dipping with dip angle of 30–40°, whereas the northwest limb is steeply dipping (~85°). Gold grades based on bulk samples vary from 1.45 g/t to 10.43 g/t.

The asymmetric M9 vein is hosted by the Jinchangxi anticline, with a moderately-dipping (26−38°) southeast limb and a more steeply-dipping (50−60°) northwest limb. Unlike the hinge zone dilation in the M7 and M8 vein, the crest of the M9 vein has a bedding-parallel lode of 20 cm thickness. Close to the anticlinal hinge on the southeast limb, where bedding dips at shallow angles, vein thickness may reach 2 m, and away from the fold hinge, bedding-parallel veins are thinner on the more steeply dipping limbs. The M9 vein has been mined for over 450 m along the fold crest and pinches out up to 60 m down-dip on each limb; grades of gold ores from bulk samples vary from 1.00 g/t to 8.60 g/t.

4. Mineralogy, alteration and paragenetic sequence

Vein mineral assemblages are dominated by quartz, which typically forms over 95% of most veins. Calcite, Fe-Mn-carbonate, chlorite and lesser quantities of sericite are present as gangue minerals (Figs. 7 and 8). The major sulfide minerals are arsenopyrite and pyrite, with minor sphalerite, galena, chalcopyrite, and rare pyrrhotite, marcasite, and tetrahedrite. Much of the gold is μm-
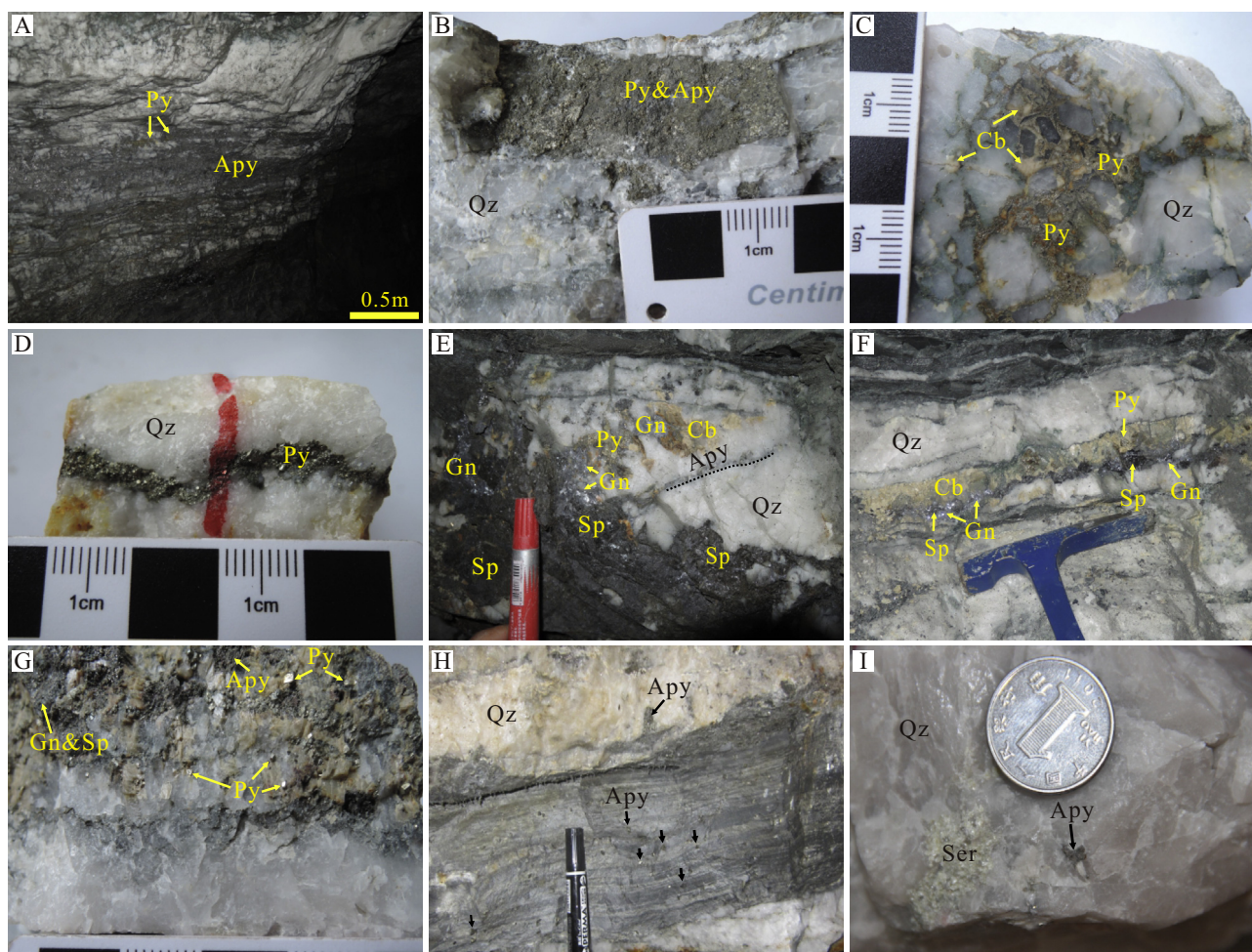
Fig. 7. Photographs showing mineral associations and textures of quartz veins. A. Arsenopyrite in stage 2 occurs as veinlets in massive quartz vein along with wall rock laminae, and pyrite occurs as aggregates locally. B. Arsenopyrite and pyrite in stage 2 occur as anhedral masses near the vein margin. C. Pyrite and carbonate from stage 4 occur as coarse aggregates in quartz vein. D. Pyrite in stage 2 occurs as veinlet in quartz vein. E. Abundant galena and sphalerite coexisting with pyrite and carbonate in quartz vein, arsenopyrite occurs as veinlet filling the fracture in the quartz, carbonate is dominated by siderite. F. Veinlet carbonate minerals intersect the stage 2 polysulfides. G. Euhedral pyrite coexists with carbonate in quartz vein, and replaces earlier arsenopyrite, galena and sphalerite. H. Alteration zone occurs immediately adjacent to quartz vein. Arsenopyrite occurs as aggregates in quartz, as well as porphyroblast in alteration zone. I. Hydrothermal sericite occurs as aggregates in quartz vein, with arsenopyrite grains nearby. Coin is 19 mm across. *Apy* arsenopyrite, *Gn* galena, *Py* pyrite, *Sp* sphalerite, *Cb* carbonate, *Ser* sericite, *Qz* quartz.

to mm-sized grains and occurs as fracture-controlled isolated grains or filaments in quartz, galena, pyrite, sphalerite, and wall-rock (Fig. 8A–C). Arsenopyrite is more abundant than pyrite and occurs as coarse, massive aggregates or veinlets throughout the quartz veins (Fig. 7A). It commonly can be seen around crack-seal fractures, along slaty laminae, and close to vein margins (Fig. 7B), as well as disseminated in altered wallrock proximal to quartz veins (Fig. 7H). Pyrite generally occurs as veinlets and aggregates in quartz veins (Fig. 7C, D), or as aggregates closely associated with arsenopyrite near the vein margins (Fig. 7B). A later generation of pyrite occurs as zoned cubes or aggregates coexisting with carbonate minerals and offsets the earlier polysulfides (Fig. 7G). Less abundant pyrite is also observed in alteration zones and can be overgrown by arsenopyrite.

The siliciclastic nature of the metasedimentary rocks has a rather limiting effect on their response to the interaction with hydrothermal fluids (Bierlein et al., 2004a). Only weak and rare hydrothermal alteration is developed in zones with less than 1–3 m in width. The alteration is characterized by the discoloration of the metasedimentary rocks, due to silicification, sericitization (Fig. 7I), and sulfidation (Fig. 7H). Sulfidation of the wallrocks is manifested by disseminated euhedral arsenopyrite and pyrite porphyroblasts (up to 2 cm) (Fig. 7H).

Based on underground mapping and petrographic study, four stages of mineralization can be distinguished as follows and the paragenetic sequence is summarized in Fig. 9.

Stage 1 sericite-pyrite-arsenopyrite-quartz

This stage produced massive milky white quartz veins that contain crack-seal fractures and thin, parallel laminae (Fig. 6B–E). This kind of crack-seal fracture formed largely as a result of variable digestion and replacement of wallrock material (Kontak and Smith, 1993). Fragments of wallrock that have been incorporated into the veins during crack-seal processes are altered to fine-grained sericite (Fig. 7H). Arsenopyrite occurs as aggregates and veinlets in the massive quartz vein, especially along the thin wall-rock laminae, or as euhedral coarse grains in the wallrock (Fig. 7G). Pyrite occurs as euhedral grains only in alteration zones, and it is overgrown by arsenopyrite.

Stage 2 gold-pyrite -quartz

This stage consists of white-grey quartz veins, containing pyrite and gold. Pyrite occurs as anhedral aggregates or veinlets, and commonly overgrows or replaces arsenopyrite (Fig. 7B, D;
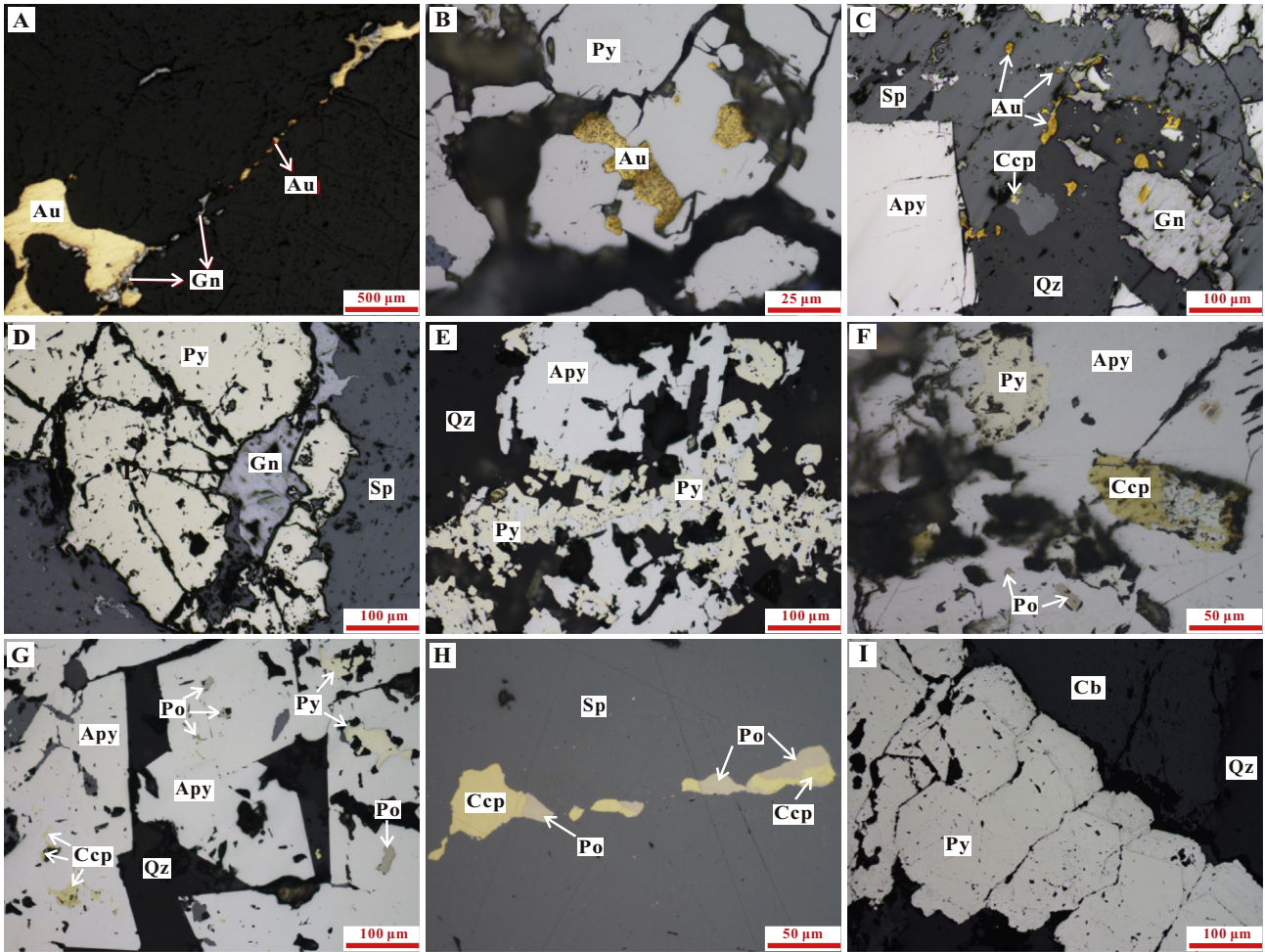
Fig. 8. Reflected-light photographs showing mineral associations and textures of sulfide minerals in gold ores. A. Irregular gold grains occur coexisting with pyrite and galena along fractures in quartz. B. Gold grains filling fractures in pyrite. C. Gold grains occur as inclusions in sphalerite, galena and quartz. D. Pyrite partially replaced by galena and sphalerite. E. Arsenopyrite cut and replaced by pyrite. F. Arsenopyrite has overgrown pyrite, and is replaced by chalcopyrite and pyrrhotite. G. Arsenopyrite replaced by pyrite, chalcopyrite and pyrrhotite. H. Chalcopyrite and pyrrhotite intergrown with sphalerite. I. Pyrite coexisting with carbonate and showing zonation. *Au* native gold, *Apy* arsenopyrite, *Ccp* chalcopyrite, *Gn* galena, *Po* pyrrhotite, *Py* pyrite, *Sp* sphalerite, *Cb* carbonate, *Ser* sericite, *Qz* quartz.

Fig. 9. Paragenetic sequence of minerals for the Pingqiu gold deposit. The widths of the solid lines define relative abundance of minerals.

Fig. 8C–G). Fine-grained gold occurs in quartz and pyrite as inclusions or along fractures in these minerals (Fig. 8A, B).

Stage 3 gold-polymetallic sulfide-quartz

Large amounts of sulfide minerals precipitated during this stage. Quartz is grey due to recrystallization and inclusions of tiny sulfide minerals. Galena, sphalerite, and chalcopyrite occur as aggregates mainly at the hinge zones and intersect or overgrow arsenopyrite and pyrite (Fig. 7E–G; Fig. 8C–H). Pyrrhotite and marcasite may partially replace pyrite and arsenopyrite (Fig. 8G, H). Native gold occurs as globular inclusions in galena, sphalerite and quartz, or fills fractures in pyrite and quartz (Fig. 8A, C).

Stage 4 pyrite-carbonate-quartz

This stage is composed of quartz, calcite, ankerite, siderite and pyrite and is only observed at the crest of anticlines. Calcite is more abundant than ankerite and both minerals occur as multiple grains and replace euhedral arsenopyrite (Fig. 7E). Pyrite is associated with siderite and shows recrystallization (Fig. 7C, E; Fig. 8I). Siderite overgrows the calcite and offsets polysulfide assemblages (Fig. 7F; Fig. 8F).

5. Samples and analytical methods

5.1. $^{40}Ar/^{39}Ar$ dating of sericite

The samples selected for dating came from the underground workings of the 700 m level and were located at the crest of the M7 vein. The massive quartz vein is milky white and has crack-seal textures and shows locally strong sericitization. Arsenopyrite is locally disseminated or occurs as aggregates within the veins. The sericite is fine-grained and has a high degree of crystallinity. The sericite dated herein is interpreted to be of hydrothermal origin as a consequence of fluid-rock interaction, accompanying formation of a high-grade gold mineralization zone.

The $^{40}Ar/^{39}Ar$ dating was carried out in the Argon Geochronology Laboratory, The University of Queensland. Sericite for incremental step-heating was prepared using the methodology outlined in Li et al. (2003, 2006). Briefly, fine-grained sericite aggregates were crushed to obtain mineral grains of uniform size (0.5–1.6 mm), and then washed in distilled water in an ultrasonic bath for 1 h, and subsequently dried. Sericite fragments were hand-picked using a binocular microscope and the purity was confirmed by XRD analysis.

Samples PQ-1 and PQ-2, along with Fish Canyon standards (28.20 Ma; Kuiper et al., 2008), were parceled in a high-purity Al disk for irradiation. The disk was irradiated for 14 h in the B-1 CLI-CIT facility at the OSU TRIGA reactor, USA. The mineral separates were step-heated with a continuous-wave Verdi Diode laser (532 nm) defocused to 2 mm, which guaranteed each grain to be heated homogeneously. Argon gas was extracted for 54–62 s at each step, and the purified gas then admitted into the MAP 215–50 mass spectrometer for argon isotopic analysis. Full system blanks and air pipettes were analyzed before and after each grain. All dates are reported using $5.543 \times 10^{-10}\,a^{-1}$ as the total decay constant for ^{40}K (Steiger and Jäger, 1977), and correction factors applied in this study are $(2.64 \pm 0.02) \times 10^{-4}$ for $(^{36}Ar/^{37}Ar)_{Ca}$, $(7.04 \pm 0.06) \times 10^{-4}$ for $(^{39}Ar/^{37}Ar)_{Ca}$ and $(8.0 \pm 3) \times 10^{-4}$ for $(^{40}Ar/^{39}Ar)_K$.

5.2. Fluid inclusion study

Twenty-six samples from various vein stages were prepared as 30-μm-thick doubly polished sections for fluid inclusion study. The samples are from both the hinge zones and limbs of the anticlines and span a vertical interval of 200 m (from 730 m level to 520 m level).

Microthermometry was performed at the China University of Geosciences using a Linkam THMS-600 heating-freezing stage. Heating rates of 1 °C/min were performed under 30 °C and 5 °C up to 400 °C. The accuracy of the measurements was ±0.2 °C during the freezing cycle and ±2 °C during heating measurements.

Laser Raman spectroscopic analyses of selected fluid inclusions were performed on a HORIBA Jobin Yvon LabRam HR Raman microspectrometer at the Institute of Geology and Geophysics, Chinese Academy of Sciences, using a 532 nm Torus laser as the excitation source and a power of 44 mW.

Quantitative analyses of CO_2, H_2S, CH_4, C_2H_4, N_2 and Ar volatile compositions as well as Cl^-, SO_4^{2-}, F^-, Na^+, K^+, Ca^{2+}, and Mg^{2+} compositions of quartz fluid inclusions were carried out at the Institute of Geology and Geophysics, Chinese Academy of Sciences. The liquid and gases were extracted from inclusions by thermal decrepitation at temperatures above 170 °C, and determined by ion chromatograph and quadrupole mass spectrometer, respectively (Zhu and Wang, 2002).

5.3. Stable isotope analyses

Six quartz samples for the oxygen and hydrogen isotope study were collected from the M7, M8 and M9 veins. Pure quartz grains, 0.25–0.425 mm in diameter, were handpicked under a binocular microscope. Analyses were carried out on a Finnigan MAT253 mass spectrometer in the Analytical Laboratory, Beijing Research Institute of Uranium Geology. Oxygen was extracted from quartz by reaction with BrF_5, and converted to CO_2 on a platinum-coated graphite rod. The hydrogen isotopic composition of fluid inclusion water was determined by decrepitating of fluid inclusions in quartz samples. The water was reduced to H_2 by passing it over a uranium metal-bearing tube and then the H_2 was transferred to the mass spectrometer. The results were reported in per mil relative to the Vienna SMOW standard for oxygen and hydrogen, and the analytical precisions were ±0.2‰ for $\delta^{18}O$ and ±2‰ for δD (Liu et al., 2013).

6. Results

6.1. $^{40}Ar/^{39}Ar$ ages

The apparent age spectra of the $^{40}Ar/^{39}Ar$ dating are listed in Table 1 and illustrated in Fig 10. Both the samples yield well-defined age plateaus with nearly 80% ^{39}Ar and plateau ages of 425.7 ± 1.7 Ma (MSWD = 2.48) and 425.2 ± 1.3 Ma (MSWD = 1.20). Both spectra display young dates in the first few, low-temperature steps, suggesting a minor amount of argon loss since crystallization of the sericite. Argon loss is also indicated by the integrated ages (422.8 ± 1.3 Ma; 423.3 ± 1.3 Ma), which are younger than the corresponding plateau ages. The stable shapes of the spectra at higher temperatures indicate that excess argon, contamination, or mixtures of multiple phases is not present in the samples.

6.2. Fluid inclusions

6.2.1. Types of fluid inclusions

Fluid inclusions are observed in massive gray and white quartz and carbonate minerals from all vein stages. The massive white quartz samples contain abundant inclusions, probably owing to repeated fracturing and healing. Three types of fluid inclusions have been identified at room temperature, based on their phase proportions and composition (Fig. 11).

Type 1 inclusions are aqueous inclusions and are the most abundant type found in this study. They can be observed in all

Table 1
^{40}Ar/^{39}Ar date of hydrothermal sericite from the Pingqiu gold deposit.

Run ID	^{40}Ar/^{39}Ar	^{36}Ar/^{39}Ar	^{37}Ar/^{39}Ar	^{38}Ar/^{39}Ar	^{40}Ar*/^{39}Ar	^{40}Ar* (%)	^{39}Ar ($\times 10^{-14}$ mol)	Age (Ma)	$\pm 1\sigma$
Sample PQ-1, J value = 0.003585									
9075-02A	57.057	0.005	0.122	0.015	55.66	97.55	0.21	328.25	3.18
9075-02B	70.885	0.002	0.001	0.013	70.35	99.25	0.91	405.76	1.57
9075-02C	73.931	0.000	0.003	0.012	74.00	100.09	2.29	424.50	0.98
9075-02D	74.447	0.000	−0.001	0.012	74.33	99.84	3.88	426.17	0.86
9075-02E	74.448	0.001	0.007	0.013	74.27	99.76	2.14	425.86	1.04
9075-02F	74.332	0.000	0.009	0.013	74.21	99.83	1.07	425.56	1.41
9075-02G	73.338	0.000	0.084	0.015	73.35	100.01	0.40	421.18	2.73
9075-02H	74.861	0.001	0.053	0.014	74.54	99.56	0.29	427.24	3.48
9075-02I	74.225	0.001	−0.011	0.013	73.91	99.57	0.32	424.03	3.22
9075-02J	75.047	0.000	0.008	0.013	75.13	100.12	0.20	430.29	3.62
9075-02K	74.977	0.001	−0.039	0.014	74.63	99.54	0.21	427.71	3.96
9075-02L	74.421	0.002	0.029	0.015	73.82	99.20	0.27	423.60	4.07
9075-02M	75.069	0.000	0.001	0.014	75.18	100.15	0.17	430.54	4.40
9075-02N	14.666	0.027	4.164	0.049	7.05	47.93	0.00	45.03	139.79
Sample PQ-2, J value = 0.003585									
9076-01A	49.591	0.035	−0.952	0.016	39.19	79.08	0.04	237.17	12.41
9076-01B	60.768	0.005	0.057	0.012	59.27	97.53	0.26	347.60	3.08
9076-01C	70.336	0.003	−0.031	0.012	69.52	98.85	0.70	401.47	1.70
9076-01D	72.996	0.002	−0.005	0.012	72.48	99.30	1.28	416.72	1.23
9076-01E	74.397	0.001	−0.001	0.012	74.14	99.65	1.90	425.21	1.10
9076-01F	74.016	0.001	−0.004	0.012	73.85	99.78	2.93	423.74	0.89
9076-01G	74.360	0.000	−0.008	0.012	74.25	99.85	4.88	425.76	0.77
9076-01H	74.280	0.001	−0.004	0.012	73.98	99.59	1.80	424.38	1.27
9076-01I	74.511	0.002	−0.005	0.013	73.93	99.23	1.17	424.17	1.81
9076-01J	75.450	0.002	−0.032	0.013	74.89	99.26	0.70	429.02	2.26
9076-01K	74.763	0.001	−0.011	0.012	74.57	99.74	0.75	427.40	1.82
9076-01L	74.801	0.001	−0.022	0.011	74.54	99.65	1.02	427.26	1.67
9076-01M	40.393	0.097	2.016	0.003	11.54	28.52	0.01	73.10	58.53
9076-01N	44.998	0.096	1.663	0.002	16.50	36.63	0.00	103.69	145.53
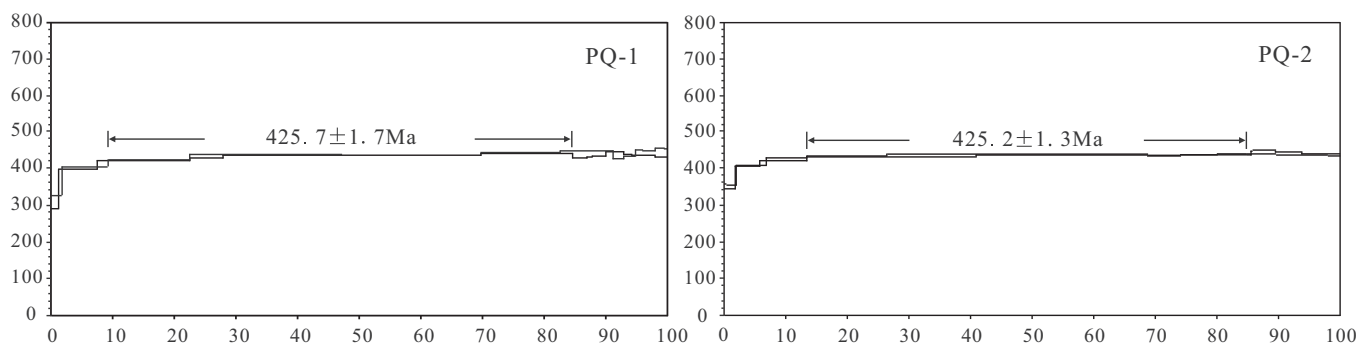
Fig. 10. Laser incremental heating ^{40}Ar/^{39}Ar age spectra of two hydrothermal sericite samples from the Pingqiu deposit.

samples investigated. The inclusions occur isolated, in clusters, or in linear arrays, and may be primary, pseudosecondary, or secondary. They are typically oval to irregular in shape, and range from ca. 3 to 12 μm across (Fig. 11A–F). Type 1 inclusions can be subdivided into one phase (type 1a) and two phase (liquid water and water vapor, type 1b), with variable proportions of liquid and vapor phases, ranging from 5% to 25%.

Type 2 inclusions are aqueous-carbonic inclusions, containing between 35% and 75% CO_2 of the total inclusion volume, and they occur as irregular shapes with angular to roundish outlines. They are less abundant than type 1 inclusions, and commonly occur in certain areas along with type 1 inclusions (Fig. 11B–F). Type 2 inclusions are slightly larger than type 1 inclusions, and generally range from 5 to 15 μm in diameter.

Type 3 inclusions are dark, one-phase carbonic inclusions that range in diameter from 2 to 10 μm. They occur as individual, isolated inclusions together with aqueous and aqueous-carbonic inclusions, and typically have negative crystal or subrounded shapes (Fig. 11E, F). These inclusions have variable relative content of CO_2 and CH_4, with minor amounts of N_2, and H_2O (Fig. 13A, B). These inclusions are too small to measure microthermometry.

A group of fluid inclusions is trapped synchronously and therefore represent a true fluid inclusion assemblage (FIA) if the inclusions were trapped along the same primary growth zone of host crystal or along the same healed fracture (Goldstein, 2001; Chi and Lu, 2008; Li et al., 2012). In the Pingqiu deposit, two types of FIAs are recognized, i.e., (1) carbonic fluid inclusion assemblage including type 2 and type 3 inclusions (Fig. 11D) and (2) aqueous fluid inclusion assemblage only consisting of type 1 inclusions (Fig. 11A).

6.2.2. Microthermometry

Microthermometric results are graphically illustrated in Fig 12. Two-phase aqueous inclusions (Type 1) yield a wide range of homogenization temperatures from 171 °C to 396 °C, with most
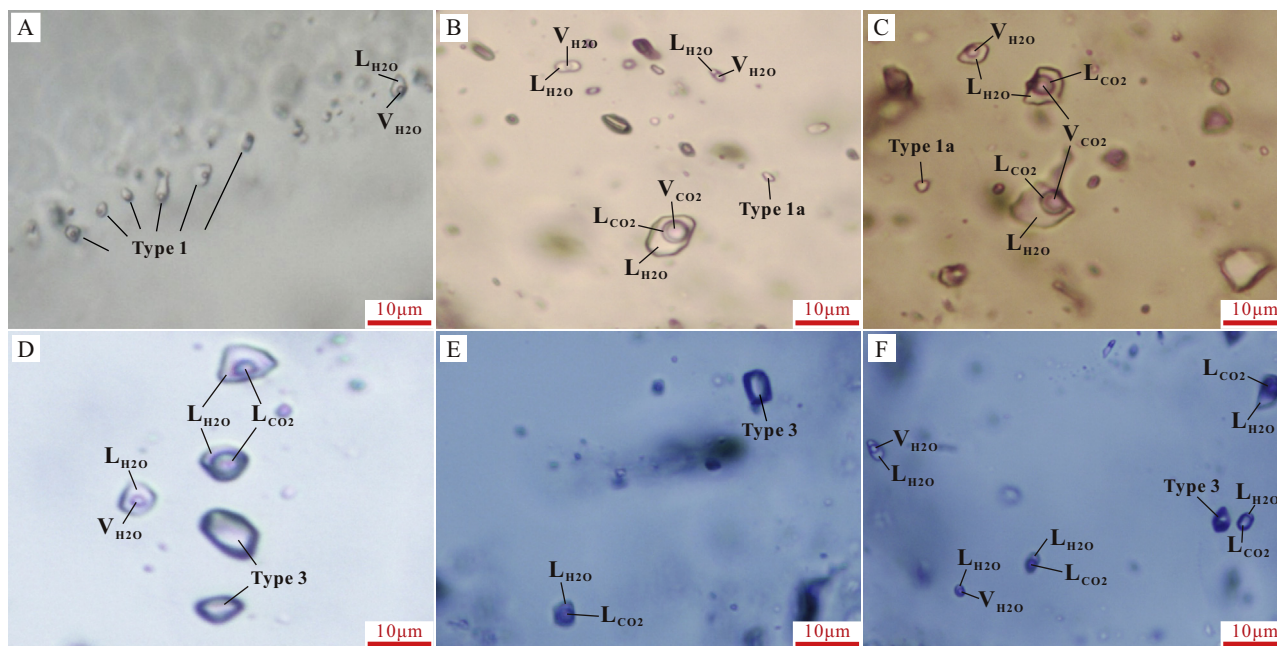
Fig. 11. Micrographs showing the types and distribution of fluid inclusions in quartz. A. Primary cluster of aqueous, liquid-rich inclusions. B. Coexisting three-phase aqueous-carbonic and two-phase aqueous inclusions. C. Three-phase aqueous-carbonic inclusions coexisting with two-phase aqueous inclusions and one-phase aqueous inclusions. D. Two-phase aqueous-carbonic coexisting with two-phase aqueous inclusions and one-phase aqueous inclusions. E. Isolated one-phase carbonic inclusion. F. One-phase carbonic inclusion coexisting with two-phase aqueous-carbonic inclusion and two-phase aqueous inclusion. L_{H2O} liquid H_2O, V_{H2O} vapor H_2O, L_{CO2} liquid CO_2, V_{CO2} vapor CO_2.

values lying between 210 °C to 310 °C (Fig. 12D); their ice melting temperatures vary from −0.8 °C to −6.5 °C (Fig. 12E). For the three-phase aqueous-carbonic inclusions (Type 2), final melting temperatures of solid CO_2 range from −61.5 °C to −56.7 °C (Fig. 12A), indicating the presence of other minor gases such as CH_4 or N_2. Clathrate melting occurs between 5.8 °C and 9.9 °C (Fig. 12C). Partial homogenization of the carbonic phase to liquid occurs between 19.5 °C and 30.5 °C (Fig. 12B), whereas those that homogenized to the vapor phase vary from 24.8 °C to 29.8 °C (Fig. 12B). The final homogenization temperatures vary from 187 °C to 350 °C (Fig. 12D).

The calculated salinities for aqueous inclusions are 1.4–9.86 wt % NaCl equiv using the equation suggested by Bodnar (1993), and those for the aqueous-carbonic inclusions fall between 0.2 and 7.7 wt% NaCl equiv using the melting temperatures of clathrate (Collins, 1979) (Fig. 12F). Carbonic phase densities and bulk densities of the three-phase aqueous-carbonic inclusions were calculated from microthermometric data using the Flincor program (Brown, 1989) and the equation of Brown and Lamb (1989). For type 2 three-phase aqueous-carbonic inclusions, CO_2 densities are 0.24–0.78 g/cm³, and bulk densities are 0.77–0.95 g/cm³. Bulk densities of the type 1b two-phase aqueous inclusions were calculated using the HokieFlincs_H₂O-NaCl program (Steele-MacInnis et al., 2012), suggesting that these inclusions have densities at 0.52–0.94 g/cm³.

6.3. Hydrothermal fluid compositions

Laser Raman spectroscopic analyses of representative fluid inclusions show that H_2O is the dominant liquid phase with minor amounts of CO_2 (Fig. 13). This corroborates microthermometric results that show melting temperatures of solid CO_2 that are lower than −56.6 °C.

Bulk analysis data of vapor bubble compositions are listed in Table 2. The results indicate that the gas phase of fluid inclusions is dominated by H_2O (91.1–98.39 mol%), followed by CO_2 (1.43–

8.42 mol%). The N_2 contents range from 0.06 mol% to 0.21 mol%, and the CH_4 contents show a similar concentration range from 0.07 mol% to 0.19 mol%. Trace amounts of C_2H_6 have been detected ranging from 0.01 mol% to 0.05 mol%. No significant H_2S was found in the vapor phases. The CO_2 contents show a negative correlation with the H_2O contents, whereas CO_2 contents have positive correlations with N_2, CH_4 and C_2H_6 concentrations.

Bulk compositions of the liquid phases are listed in Table 2. The Na^+ contents vary widely from 4.86 μg/g to 16.30 μg/g, and the Ca^{2+} contents vary from 0.24 μg/g to 1.08 μg/g. Neither significant K^+ nor Mg^{2+} has been detected. The Cl^- concentrations broadly range from 3.15 μg/g to 22.50 μg/g, whereas the SO_4^{2-} concentrations are more uniform ranging from 6.00 μg/g to 7.35 μg/g. No significant F^- has been detected.

The analytical results presented above show that the fluid inclusions contain at least the following 9 components: H_2O, CO_2, N_2, CH_4, Ar, Na^+, Ca^{2+}, Cl^-, and SO_4^{2-}.

6.4. Stable isotope analyses

Hydrogen and oxygen isotope data are shown in Table 3. The measured $\delta^{18}O$ values of quartz samples fall between +12.8‰ and +15.9‰. Calculated $\delta^{18}O$ values of the fluid in equilibrium with quartz range from 4.3‰ to 8.3‰, using the equation of Clayton et al. (1972), and the corresponding primary fluid inclusion homogenization temperatures of the same samples. Fluid inclusion δD values vary from −55.8 to −46.9‰.

7. Discussion

7.1. Timing of gold mineralization

It is important to select samples for $^{40}Ar/^{39}Ar$ geochronology that contain a single, dominant population of sufficiently coarse-grained hydrothermal micas, with a minimum of detrital components (Phillips et al., 2012). Although sericite could be generated
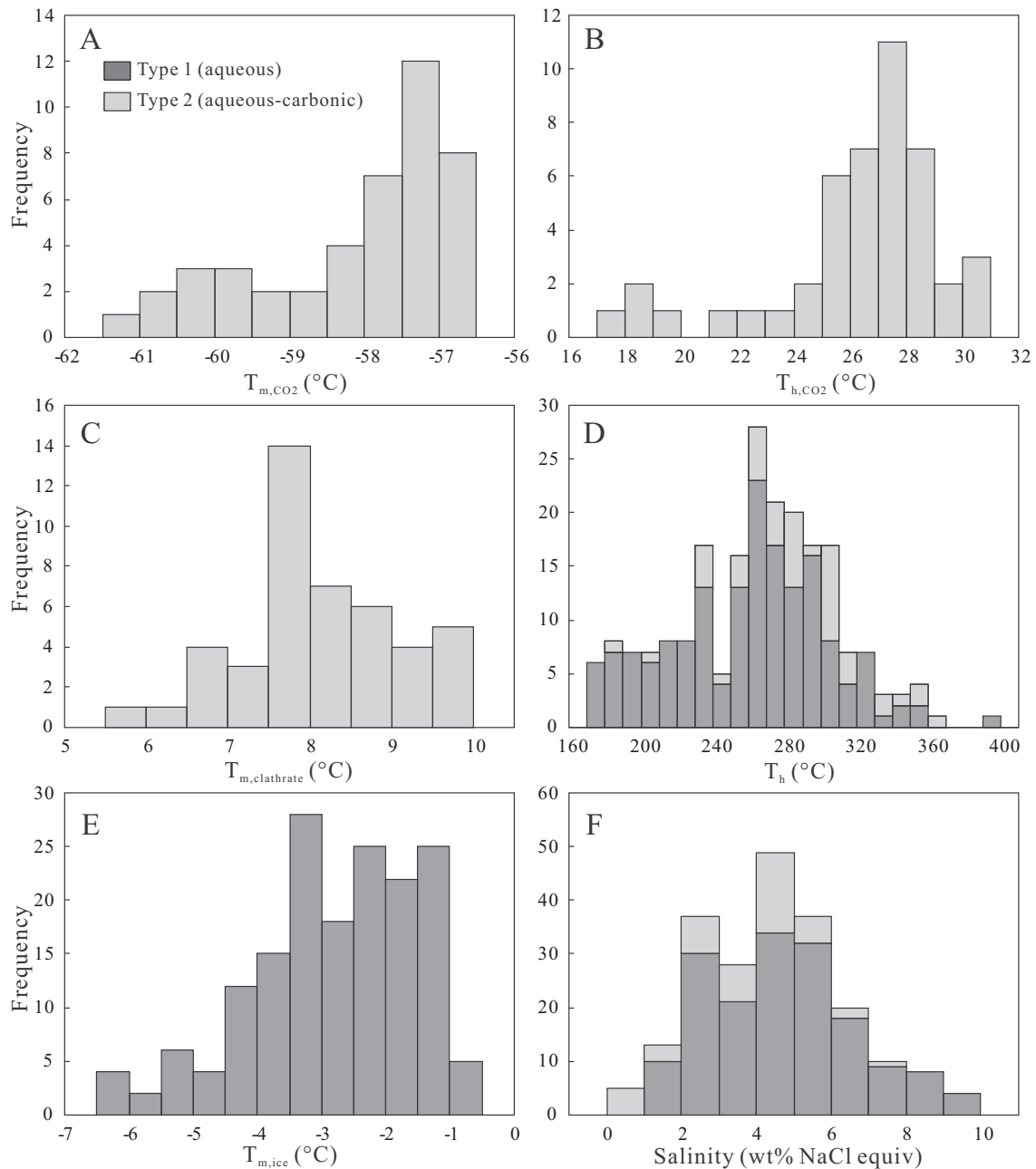
Fig. 12. Histograms of microthermometric data (A–E) and calculated salinity (F) for three-phase aqueous-carbonic and two-phase aqueous inclusions. A. CO_2 melting temperature. B. Partial homogenization temperature of CO_2. C. Clathrate melting temperature. D. Total homogenization temperature. E. Ice melting temperature of aqueous inclusions. F. Calculated salinity for three-phase aqueous-carbonic and two-phase aqueous inclusions.

during regional metamorphism, such grains at Pingqiu are aligned parallel to fold axial surfaces and typically much smaller (generally <1 μm in thickness) compared to the hydrothermal sericite (fine-grained muscovite). The hydrothermal sericite dated in this study displays a close relationship with gold-bearing sulfide minerals and are interpreted to be of hydrothermal origin. Microthermometry of fluid inclusions in auriferous quartz lodes at Pingqiu yielded final homogenization temperatures between 171 °C and 396 °C, broadly equivalent to, or only marginally hotter than the sericite closure temperature for Ar retention of 270–350 °C (Jäger, 1979; Lister and Baldwin, 1996; McDougall and Harrison, 1999), which potentially could have reset the argon signature to the time of gold mineralization. Alternatively, destruction of the iron-rich chlorite in wallrocks during hydrothermal alteration can generate

hydrothermal sericite (Bierlein et al., 1998, 2000), which also would record the time of gold mineralization. Both analyzed samples yielded stable and concordant plateaus, indicating the samples comprised essentially a single generation of sericite, and that sericite was not heated above its closure temperature during subsequent events (Arehart et al., 2003; Hall et al., 2000). Thus, we advocate that these two $^{40}Ar/^{39}Ar$ ages directly date the hydrothermal alteration and, by inference, gold mineralization.

Our new $^{40}Ar/^{39}Ar$ data show that gold mineralization formed at ca. 425 Ma and closely followed the main tectonic events of the Caledonian orogeny. BGMRGZP (1987), Dai et al. (2005, 2013) and Lu et al. (2005) pointed out that vein-bearing folds and faults were formed as the compressional product of the Caledonian orogeny in the Jiangnan Belt. As compression developed, the turbidite
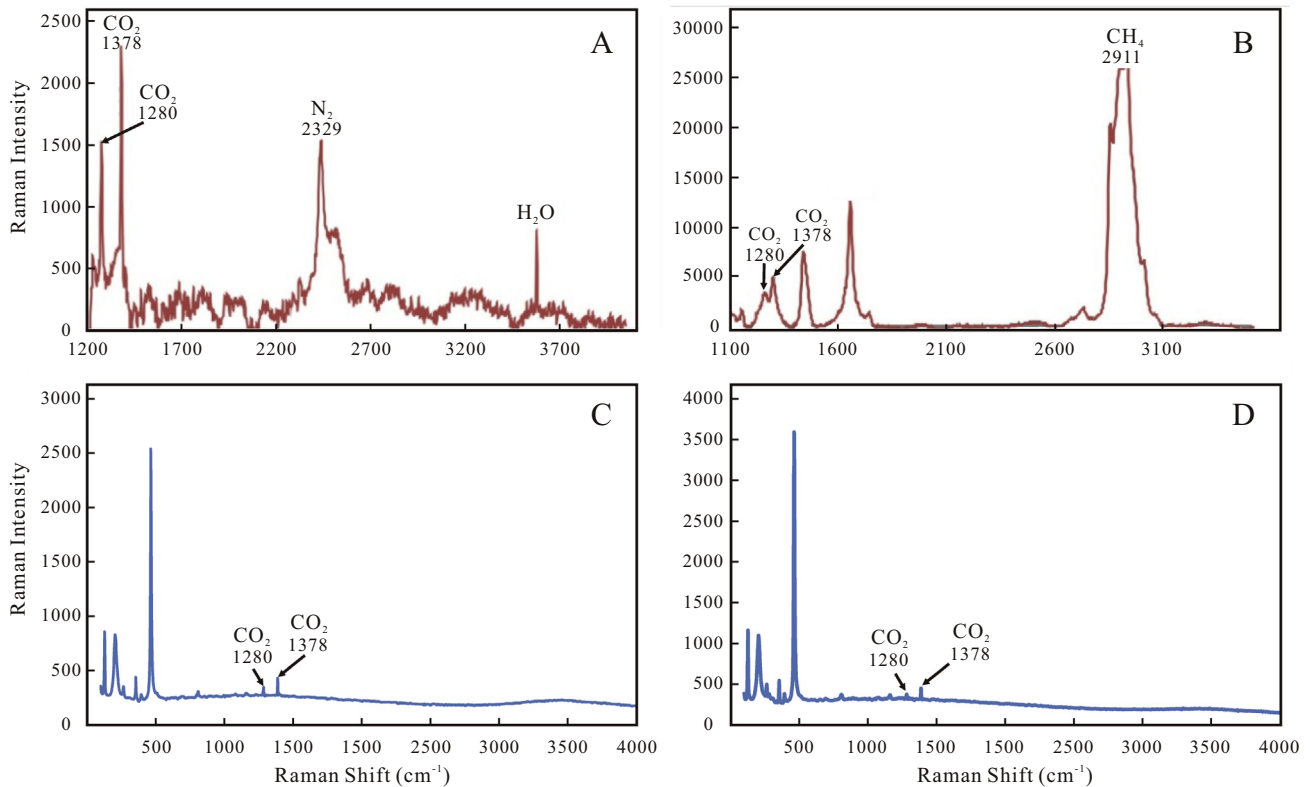
Fig. 13. Raman spectra of carbonic, aqueous-carbonic and aqueous inclusions. A. Carbonic inclusions (type 3) consist predominantly of CO_2, with minor amounts of CH_4 and H_2O. B. Carbonic inclusions contain mainly CH_4 and minor amounts of CO_2. C and D. Both vapor and liquid phases of the aqueous inclusions (type 1) contain minor to trace amounts of CO_2.

Table 2
Results of bulk analyses of gas and liquid phase compositions of fluid inclusions from the Pingqiu gold deposit.

Sample no.		530-4	530-6	580-7	580-11	580-14	580-18	660-4	660-7
Ore stage		1	1	2	2	2	3	3	3
Gas phase composition (mol%)	H_2O	92.24	91.10	96.75	97.23	95.61	95.76	98.39	98.18
	N_2	0.17	0.21	0.12	0.11	0.10	0.09	0.07	0.06
	Ar	0.013	0.031	0.028	0.028	0.012	0.014	0.028	0.012
	CO_2	7.40	8.42	2.98	2.44	4.18	4.03	1.43	1.68
	CH_4	0.14	0.19	0.13	0.18	0.09	0.08	0.09	0.07
	C_2H_6	0.04	0.05	0.01	0.01	0.01	0.02	0.01	0.01
	H_2O/CO_2	12.47	10.82	32.48	39.83	22.89	23.76	68.99	58.53
	$CO_2/CO_2{+}CH_4$	0.98	0.98	0.96	0.93	0.98	0.98	0.94	0.96
Liquid phase composition (µg/g)	Cl^-	21.3	14.7	3.15	7.77	14.2	17.7	10.7	22.5
	SO_4^{2-}	6.90	6.15	6.30	6.00	7.35	6.90	6.30	6.30
	Na^+	16.3	11.1	4.86	7.32	12.0	3.5	8.64	15.4
	K^+	bdl	bdl	bdl	bdl	bdl	bdl	bdl	bdl
	Mg^{2+}	bdl	bdl	bdl	bdl	bdl	bdl	bdl	bdl
	Ca^{2+}	0.42	0.36	bdl	bdl	0.24	0.36	0.48	1.08
	$\sum$	45	32.3	14.3	21.1	33.8	38.4	26.1	45.2

bdl below detection limit.

sequence buckled and further folded, followed by flexural slip along the bedding surfaces and dilation at the crest, leading to the emplacement of bedding-parallel quartz veins and saddle-reefs.

A substantial effort has been made to constrain the timing of gold mineralization in the southeastern Guizhou district and the adjacent southwestern Hunan district, including K-Ar, $^{40}Ar/^{39}Ar$, Rb-Sr, Sm-Nd and Re-Os methods (Table 4). A cluster of Rb-Sr isochron ages ranging from 492 Ma to 340 Ma has been obtained from the fluid inclusions in auriferous quartz in the southeastern Guizhou district (Zhu et al., 2006), but their significance is uncertain owing to problems interpreting Rb-Sr ages of fluid inclusions.

Peng et al. (2003) reported two $^{40}Ar/^{39}Ar$ dates of fluid inclusions extracted from auriferous quartz of the Woxi W-Sb-Au deposit that yielded plateau ages at 420 ± 20 Ma and 414 ± 19 Ma, and a scheelite Sm-Nd age at 402 ± 6 Ma. These data are in good agreement with our data for two sericite samples from the Pingqiu deposit. Two relatively young results from arsenopyrite in auriferous quartz veins at Jinjing (Re-Os, 174 ± 15 Ma; Wang et al., 2011) and fluid inclusions extracted from auriferous quartz at Woxi (Rb-Sr, 144.8 ± 11.7 Ma; Shi et al., 1993) have been interpreted to represent gold mineralization formed during the Yanshanian orogeny. Although movements during the Yanshanian orogeny strengthened the structural architecture, there is no substantial

Table 3
The $\delta^{18}O$, $\delta^{18}D$ and calculated $\delta^{18}O_{fluid}$ (‰) values from the Pingqiu gold deposit.

Sample no.	Ore stage	Mineral	Sample description	Th °C	$\delta^{18}O_Q$ ‰	$\delta^{18}O_{fluid}$ ‰	$\delta^{18}D$ ‰
530-1	1	Quartz	Py-Qz vein	280	15.9	8.3	−53.6
530-4	1	Quartz	Sp-Gn-Ccp-Py-Qz vein	280	15.4	7.8	−46.9
580-15	2	Quartz	Apy-Qz vein	270	14.1	6.0	−55.8
580-21	3	Quartz	Apy-Qz vein	270	14.7	6.6	−54.2
660-10	3	Quartz	Apy-Gn-Qz vein	260	13.0	4.5	−50.0
660-16	3	Quartz	Gn-Sp-Qz vein	260	12.8	4.3	−48.8

[1]*Apy* arsenopyrite, *Py* pyrite, *Gn* galena, *Sp* sphalerite, *Ccp* chalcopyrite, *Qz* quartz.
[2]$\delta^{18}O_{fluid}$ of ore-forming fluids in equilibrium with quartz is calculated according to the formula of $1000ln\alpha quartz-water = 3.38 \times 10^6 T^{-2}-3.40$ (Clayton et al., 1972). The temperatures used in calculations are the homogenization temperatures of the fluid inclusions observed in individual samples.

evidence supporting that significant gold mineralization took place during the Yanshanian orogeny at the southeastern Guizhou and the southwestern Hunan districts. In addition, gold mineralization of similar ages (450–400 Ma) is also well developed in Caledonian metamorphic belts in the South China Caledonian fold belt and adjacent Jiangnan rise (Wang et al., 1999; Wang and Liang, 2000; Ni et al., 2015). This suggests that gold deposits in these regions formed more or less contemporaneously and in a similar geodynamic setting.

The Caledonian tectonothermal event in the Xuefeng belt can be subdivided into three episodes, the D1 deformation formed NEE-trending upright, open to tight folds and thrust faults, and followed by a stronger, NW−SE-directed D2 deformation, led to en echelon-like, NE-trending tight folds, overturned folds and faults. The last D3 deformation is late-orogenic collapse, with a series of detachment faults (Hou et al., 1998). Two sericite samples from the ductile shear zones yielded ^{40}Ar-^{39}Ar plateau ages at 416.4 ± 1.8 Ma, 426.5 ± 2.3 Ma (Tang et al., 2014), suggesting the time of D2 deformation. Since coeval intrusions are absent and the ductile deformation is weakly developed during orogeny, the southeastern Guizhou district is interpreted to be the outer part of the orogen and is weakly affected by deep-seated tectono-metamorphic events (Dai et al., 2005; Chu et al., 2012).

Thus, we conclude that the ca. 425 Ma Ar-Ar age data on the hydrothermal sericite yields an approximate age for gold mineralization in the Pingqiu deposit, that gold mineralization post-dated peak metamorphism and was emplaced into rocks affected by lower greenschist facies metamorphism during the later stages of ongoing regional deformation.

7.2. Gold transport and deposition

Gold is predominantly transported as Au-Cl or Au-S complexes in ore-forming fluids and as a thiosulfide complex ($Au(HS)_2^-$) under greenschist and sub-greenschist facies conditions (McCuaig and Kerrich, 1998 and references therein). Gold mostly occurs as $Au(HS)_2^-$ at low salinities, low temperatures, near-neutral to weakly acidic pH, and low f_{O2} conditions (Zhu et al., 2011; Yoo et al., 2010; Fan et al., 2003). Chemical modeling indicates that $Au(HS)_2^-$ is the dominant species under neutral pH conditions typically found in turbidite-hosted gold deposits (Mernagh and Bierlein, 2008). The absence of K-feldspar and the presence of white mica in alteration zones and the stability of carbonate minerals indicate near-neutral to slightly alkaline conditions for the ore-forming fluids, with pH values falling between 5.0 and 6.2 (Mikucki and Ridley, 1993). The lack of sulfate minerals and hematite, and arsenopyrite as the major sulfide within the gold district, indicate reducing nature of the fluids (Downes et al., 2008; Yoo et al., 2010). Estimated pH of the ore-forming fluids at the Moshan deposit in the southeastern Guizhou district yielded 6.6 to 7.1 (Zhang, 2001). Hence, at the physico-chemical conditions discussed above, it is likely that HS^- is the dominant sulfur species

in the gold ore-forming fluids and gold is transported dominantly as the $Au(HS)_2^-$ complex.

Gold deposition from $Au(HS)_2^-$ may be caused by several mechanisms, including pH change, f_{O2} change, $\sum S$ change, and boiling, cooling, oxidation, or reduction of the fluids (Hayashi and Ohmoto, 1991; McCuaig and Kerrich, 1998; Klein et al., 2006; Yoo et al., 2010). Rapid cooling of the fluids can be ruled out at the deposit scale, and a drastic change in pH is also unlikely to have occurred at Pingqiu because of the limited extent of wallrock alteration. Sulfidation of the wallrocks commonly increases fluid f_{O2} and reduces f_{S2}. This has been demonstrated as an efficient gold deposition mechanism in lode deposits (Neall and Phillips, 1987). In the Pingqiu deposit, native gold grains locally occur at the contact between the quartz veins and the host rocks, and gold shows a close relationship with Fe-sulfide minerals, pointing to the importance of a wallrock sulfidation model. However, the sulfide content in the alteration zone is low, and gold contents in the largely non-reactive wallrocks are subordinate compared to within the quartz veins, suggesting that wallrock sulfidation is not the major factor in gold precipitation. Chemical modeling suggested that gold precipitation is associated with desulfidation of the fluid and is generally accompanied by phase separation (Mernagh and Bierlein, 2008). At the Pingqiu gold deposit, the coexistence of carbonic, aqueous, and aqueous-carbonic fluid inclusions with various vapor/liquid ratios (Fig. 11) indicates that they have been trapped contemporaneously. Aqueous-carbonic fluid inclusions with different carbonic-phase/H_2O ratios have been observed to homogenize both to liquid and vapor phases within the same range of temperatures. Generally, the final homogenization temperatures of aqueous-carbonic inclusions are slightly hotter than the aqueous inclusions, whereas the salinities of the latter are slightly higher than the water phase in aqueous-carbonic inclusions. These characteristics satisfy at least some of the criteria proposed by Ramboz et al. (1982) to identify fluid immiscibility. Therefore, fluid immiscibility may have triggered gold deposition in quartz veins. The CO_2, CH_4, and other gases would have been partitioned into the vapor phase, resulting in destabilization of $Au(HS)_2^-$, and precipitation of gold. Decompression is considered most likely to cause phase separation in metasedimentary rock-hosted deposits where evidence of hydrofracturing is clearly present (Mernagh and Bierlein, 2008).

Thus, we conclude that at the Pingqiu gold deposit, gold is mainly transported as the $Au(HS)_2^-$ complex, and the sulfidation of the wallrocks controls the gold deposition in wallrocks, whereas fluid immiscibility triggered the main gold precipitation in quartz veins.

7.3. Source of ore-forming fluids

The δD and $\delta^{18}O$ values of vein quartz and the calculated $\delta^{18}O_{H2O}$ values from the Pingqiu gold deposit fall into the range of values shared by most orogenic gold deposits (Chen et al.,

Table 4
Previous radiometric age data of the turbidite-hosted gold deposits in southeastern Guizhou and southwestern Hunan districts.

Deposit	Host rock	Sample	Method	Age/Ma	Reference
Xiaojia	Neoproterozoic Jiangkou Fm.	Fluid inclusions in auriferous quartz Altered rocks	Rb-Sr isochron	412 ± 33 418 ± 4	Peng and Dai, 1998
Pingcha	Neoproterozoic Jiangkou Fm.	Fluid inclusions in auriferous quartz	Rb-Sr isochron	435 ± 9	
Mobin	Neoproterozoic Wuqiangxi Fm.	Potassium feldspar	K-Ar	404.20	Wang et al., 1999
Liulincha	Neoproterozoic Wuqiangxi Fm.	Potassium feldspar	K-Ar	412.46	Wang et al., 1999
Woxi	Neoproterozoic Madiyi Fm.	Altered rocks	K-Ar	281	Luo, 1989
		Fluid inclusions in auriferous quartz	Rb-Sr isochron	144.8 ± 11.7	Shi et al., 1993
		Scheelite	Sm-Nd isochron	402 ± 6	Peng et al., 2003
		Fluid inclusions in auriferous quartz	^{40}Ar/^{39}Ar	420 ± 20 414 ± 19	
Yangwantuan	Neoproterozoic Qingshuijiang Fm.	Fluid inclusions in auriferous quartz	^{40}Ar/^{39}Ar	381.7 ± 0.4	
Jintou	Neoproterozoic Longli Fm.	Fluid inclusions in auriferous quartz	Rb-Sr isochron	430 ± 44 (MSWD = 187)	Zhu et al., 2006
Tonggu	Neoproterozoic Longli Fm.	Fluid inclusions in auriferous quartz	Rb-Sr isochron	425 ± 16 (MSWD = 2187)	
Pingqiu	Neoproterozoic Fanzhao Fm.	Fluid inclusions in auriferous quartz	Rb-Sr isochron	492 ± 37 (MSWD = 191) 477 ± 14 (MSWS = 414)	
		Arsenopyrite	Re-Os isochron	400 ± 24 (MSWD = 0.96)	Wang et al., 2011
Jinjing	Neoproterozoic Qingshuijiang Fm.	Arsenopyrite	Re-Os isochron	174 ± 15 (MSWD = 1.07)	
		Fluid inclusions in auriferous quartz	Rb-Sr isochron	340 ± 16 (MSWD = 0.71)	Zhu et al., 2006

Three dates from the Mobin, Liulincha and Woxi deposits are lacking errors because they are not provided in the original.

2012; Ridley and Diamond, 2000; Jia et al., 2001, and references therein). The δD and calculated $\delta^{18}O_{H2O}$ of ore-forming fluids cluster tightly, and overlap the magmatic and metamorphic field in Fig. 14, making an unequivocal interpretation about the fluid source impossible based on the oxygen and hydrogen isotope data.

Initial ore-forming fluids at the Pingqiu gold deposit are aqueous-carbonic with X_{CO2} of 0.03–0.13 and salinities of 0.2–9.8 wt.% NaCl equiv, which corresponds to the composition of ore-forming fluids in many orogenic gold deposits globally (see e.g., Chen, 2006; Goldfarb et al., 2001; Goldfarb and Groves, 2015), and appears to be typical for low-grade metamorphic rocks,
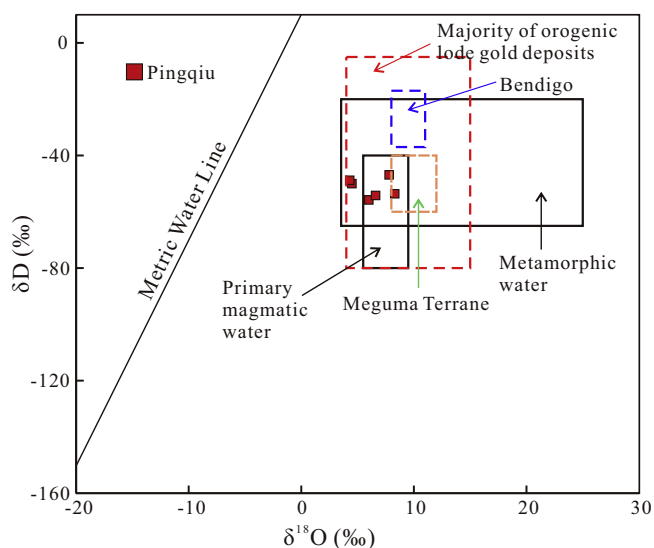
Fig. 14. Calculated $\delta^{18}O$ and δD values of fluids at Pingqiu. Domains for metamorphic and magmatic fluids are cited from Taylor (1997), and domains for majority of orogenic lode gold deposits, Bendigo and Meguma Terrane are after Ridley and Diamond (2000), Jia et al. (2001) and Kontak (1996), respectively.

but differs remarkably from the characteristics of magmatic fluids (Chen et al., 2007). Lu et al. (2006) and Wu et al. (2015), based on H-O isotopes, propose a magmatic fluid origin for the Pingqiu deposit. However, no coeval granitic intrusions have been documented in the southeastern Guizhou district. Granitoids and diabase have been reported ~100 km away from the Pingqiu gold deposit in the south margin and to the north of this district, but robust geochronology indicates that they are invariably older than the gold mineralization (Zeng et al., 2005; Fan et al., 2010; Wang et al., 2012; Chen et al., 2014). Although Caledonian granitoids (ca. 400–460 Ma) have been reported in the adjacent western Hunan district (Bai et al., 2015), they show neither intimate spatial nor genetic association with the gold mineralization at the Woxi and Mobin gold deposits (Peng et al., 2000; Song, 2014). Thus, a magmatic-hydrothermal model can be excluded to explain fluid source.

The metamorphic devolatilization model for orogenic gold mineralization appears to explain the origin of the gold in the Pingqiu deposit. Calculations using phase equilibria in the simplified system $Na_2O-CaO-FeO-MgO-Al_2O_3-H_2O-CO_2$ have shown that hydrous and carbonate minerals at mid-crustal level will break down, thus large amounts of auriferous $H_2O-H_2S\pm CO_2$ fluids are produced, mostly within the temperature range of 500–550 °C (Phillips and Powell, 2010; Tomkins, 2013). The Pingqiu gold deposit has experienced extensive regional greenschist facies metamorphism and NE-trending deformation, and the auriferous veins are strictly hosted in the folds and related faults. Consequently, the mineralizing fluids are likely generated by metamorphic devolatilization.

7.4. Comparison between Pingqiu and similar gold deposits and implications for exploration

Both the western Lachlan Belt in central Victoria, Australia and the Meguma Terrane in Nova Scotia, Canada host a cluster of economically significant turbidite-hosted gold deposits and are among

Table 5
Comparison of principal characteristics of Pingqiu, Bendigo, and Dufferin.

Principal characteristics	Pingqiu	Bendigo	Dufferin
Host Rocks	Tuffaceous-rich metasandstone, metasiltstone, and slate	Sandstone, siltstone and shale	Metasandstone with lesser metasiltstone and slate
Age of host turbidite	Neoproterozoic	Lower and Middle Ordovician	Cambrian
Regional peak metamorphism	Lower greenschist	Sub-greenschist to lower amphibolite	Lower greenschist to upper amphibolite
Regional magmatism	None	Post-tectonic mafic-felsic intrusives emplaced at 420–400 and 380–370 Ma	Peraluminous granitoids, minor gabbroic intrusions and lamprophyre dykes emplaced at 375–370 Ma; Early Jurassic lamprophyres
Distance to intrusions	>80 km	The sequence around Bendigo is intruded by the Harcourt hornblende granodiorite	>10 km
Age of mineralization	*ca* 425 Ma	*ca* 445 Ma	*ca* 380 Ma
Historical Au production (in tonnes)	>3 (2007)	529 (1992)	12 (1987)
Vein morphology	Saddle reefs, discordant veins	Saddle reefs, discordant veins	Saddle reefs and their down limb extensions, with lesser en echelon and discordant veins
Sulfide association	Arsenopyrite and pyrite, with minor sphalerite, galena, chalcopyrite, and rare pyrrhotite, marcasite, and tetrahedrite	Arsenopyrite, pyrite, galena, sphalerite with minor chalcopyrite, and pyrrhotite	Arsenopyrite with variable amounts of pyrrhotite, pyrite, chalcopyrite, galena, and rare sphalerite and molybdenite
Wallrock alteration	Silicification, sericitization, sulfidization	Silicification, carbonatization with carbonate spotting, sulfidization	Silicification, sulfidization, carbonatization, sericitization
Fluid chemistry	H_2O-CO_2-CH_4-NaCl, 0–10 wt.% equiv. NaCl, T_h 170–400 °C, 2–3 kbars, $\delta^{18}O$:15.9–17.2‰	H_2O-CO_2-CH_4-NaCl, 0–12 wt.% equiv. NaCl, T_h 200–400 °C, 2–3 kbars, $\delta^{18}O$:15.9–17.2‰	H_2O-CO_2-CH_4-NaCl, 5–8 wt.% equiv. NaCl, T_h 350–400 °C, 2–3 kbars, $\delta^{18}O$:10.4–11.6‰

the world's most productive gold areas (Bierlein et al., 2004b; Kontak et al., 1990; Ryan and Smith, 1998; Lu et al., 2008; Ramsay et al., 1998; Cox et al., 1991; Wilson et al., 2013; Kontak et al., 2011; Lisitsin and Pitcairn, 2016; Kretschmar and McBride, 2015). A comparison of principal characteristics between Pingqiu, Bendigo and Dufferin is shown in Table 5, illustrating the similarities and differences between Pingqiu and typical gold mines in those two fold belts. The Bendigo goldfield is the largest in Victoria and has produced 529 metric tons of vein-hosted gold (Willman and Wilkinson, 1992). The Dufferin gold deposit represents one of the best examples of saddle-reef vein types of the Meguma gold deposits and it has been mined successfully on a small scale (Morelli et al., 2005; Sangster and Smith, 2007). It is obvious that the principle differences between Pingqiu and the other two deposits relate to the variations in the (1) age of the wallrock protoliths; (2) relative timing of regional metamorphism, magma intrusion and vein formation; (3) physico-chemical conditions of the ore-forming fluids. These differences follow those summarized by Bierlein et al., 2004b between the central Victoria, the Buller Terrane, and the Meguma Terrane, and may lead to the disparity in overall gold endowment.

However, equally plausible for the gold disparity is the fact that the general lack of exploration in the Pingqiu. In spite of the variations summarized above, these deposits share similar structural make-up, which are represented by chevron-style folds, and auriferous veins are dominated by saddle-reefs with extensions along strike. In the Dufferin deposit, extensive exploration led to the discovery of two saddle-reef vein arrays approximately 700 m along strike and a third saddle-reef vein array at depth (Horne and Jodrey, 2001). Therefore, potential for further discoveries of saddle-reefs at depth can be expected in the Pingqiu on the basis of the fold geometry.

8. Conclusions

1. The Pingqiu gold deposit is hosted by tuffaceous metasandstone and metasiltstone of the Neoproterozoic Fanzhao Formation, and is controlled by fold-related structures. Veins are asymmetric and crest-shaped, with bedding-parallel laminated veins on limbs and thickened hinge zones. Bedding-discordant veins are dominantly developed at the hinge zones. The mineralization can be divided into four stages, i.e., sericite-pyrite-arsenopyrite-quartz veins, gold-pyrite-quartz veins, gold-polysulfide-quartz veins, and pyrite-carbonate-quartz veins.

2. Fluid inclusion petrography and microthermometric data suggest that aqueous, aqueous-carbonic and carbonic inclusions are present in the quartz. Aqueous-carbonic inclusions have salinities of 0.2 and 7.7 wt% NaCl equiv and final homogenization temperatures of 187–350 °C. Aqueous inclusions yield salinities of 1.4–9.86 wt% NaCl equiv and homogenization temperatures of 171–396 °C. The close association of CO_2-rich inclusions and H_2O-rich inclusions in clusters and along the same trails suggest that fluid immiscibility took place during mineralization.

3. $Au(HS)_2^-$ is interpreted to be the dominant complex that transported the gold at Pingqiu. The sulfidation of the wallrocks controlled gold deposition in wallrocks, whereas fluid immiscibility triggered the main gold precipitation in quartz veins.

4. Given the consistence of lower greenschist facies regional metamorphism, final homogenization temperatures of ore-forming fluids, and the closure temperature for argon reset in sericite, the well-defined $^{40}Ar/^{39}Ar$ plateau ages, combined with other well-constrained ages of mineralization and structural movements, suggest that the gold mineralization post-dated peak metamorphism and was emplaced during the later stages of ongoing regional deformation. No coeval and causative granites have been documented in this region. The geological background, the hydrogen and oxygen isotopes of fluid inclusions, and analogies with other similar deposit types, indicate that the ore-forming fluids are metamorphic in origin and interacted with the surrounding metasediments as revealed by the sulfidation in the wall rocks.

5. The Pingqiu gold deposit is similar to but also different from the representative Bendigo goldfield in the central Victorian and the Dufferin deposit in the Meguma Terrane. Principle differences relate to the variations in the (1) age of the wallrock protoliths; (2) relative timing of regional metamorphism, magma intrusion and vein formation; and (3) physico-chemical conditions of the ore-forming fluids. The remarkable similarities in structural make-up may have implications for gold exploration.

Acknowledgements

References

Arehart, G.B., Chakurian, A.M., Tretbar, D.R., Christensen, J.N., McInnes, B.A., Donelic, R.A., 2003. Evaluation of radioisotope dating of Carlin-type deposits in the Great Basin, western North America, and implications for deposit genesis. Econ. Geol. 98, 235–248.

Bai, D.Y., Zhong, X., Jia, P.Y., Xiong, X., Huang, W.Y., Jiang, W., 2015. Progress in the deformations and tetonic evolutions of the Xuefeng orogenic Belt and its adjacent areas. Geol. Miner. Resour. South China 31, 321–343 (in Chinese with English abstract).

Bierlein, F.P., Arne, D.C., McKnight, S., Lu, J., Reeves, S., Besanko, J., Cooke, D., 2000. Wall-rock petrology and geochemistry in alteration halos associated with mesothermal gold mineralization, central Victoria, Australia. Econ. Geol. 95, 283–311.

Bierlein, F.P., Fuller, T., Stüwe, K., Arne, D.C., Keays, R.R., 1998. Wallrock alteration associated with turbidite-hosted gold deposits. Examples from the Palaeozoic Lachlan Fold Belt in central Victoria, Australia. Ore Geol. Rev. 13, 345–380.

Bierlein, F.P., Arne, D.C., Cartwright, I., 2004a. Stable isotope (C, O, S) systematics in alteration haloes associated with orogenic gold mineralization in the Victorian gold province, SE Australia. Geochem.: Explor. Environ., Anal. 4, 191–211.

Bierlein, F.P., Christie, A.B., Smith, P.K., 2004b. A comparison of orogenic gold mineralisation in central Victoria (AUS), western South Island (NZ) and Nova Scotia (CAN): implications for variations in the endowment of Palaeozoic metamorphic terrains. Ore Geol. Rev. 25, 125–168.

Bodnar, R.J., 1993. Revised equation and table for determining the freezing point depression of H_2O-NaCl solutions. Geochim. Cosmochim. Acta 57, 683–684.

Brown, P.E., 1989. FLINCOR: a microcomputer program for the reduction and investigation of fluid-inclusion data. Am. Mineral. 74, 1390–1393.

Brown, P.E., Lamb, W.M., 1989. P-V-T properties of fluids in the system $H_2O \pm CO_2 \pm NaCl$: new graphical presentations and implications for fluid inclusion studies. Geochim. Cosmochim. Acta 53, 1209–1221.

Bureau of Geology and Mineral Resources of Guizhou Province (BGMRGZP), 1987. Regional Geology of Guizhou Province. Geological Publishing House, Beijing (in Chinese).

Bureau of Geology and Mineral Resources of Guizhou Province, 2012. Regional Geology of Guizhou Province. Geological Publishing House, Beijing (in Chinese).

Chen, H.Y., Chen, Y.J., Baker, M., 2012. Isotopic geochemistry of the Sawayaerdun orogenic-type gold deposit, Tianshan, northwest China: implications for ore genesis and mineral exploration. Chem. Geol. 310, 1–11.

Chen, J.S., Dai, C.G., Peng, C.L., Yang, K.D., Wang, M., Lu, D.B., 2014. Characteristics and geological implications of the Xiajiangian (Neoproterozoic) granite porphyry in the Congjiang region, southeastern Guizhou. Sediment. Geol. Tethyan Geol. 34, 61–71 (in Chinese with English abstract).

Chen, W.Y., Lu, H.Z., Wang, Z.G., Hu, R.Z., Wu, X.Y., Keita, M., Zhu, X.Q., 2006. Preliminary study on relationship between volcaniclastic turbidites and gold deposits of the Xiajiang Group of Neoproterozoic Qingbaikouan in southeastern Guizhou Province. J. Palaeogeogr. 4, 487–497 (in Chinese with English abstract).

Chen, Y.J., 2006. Orogenic-type deposits and their metallogenic model and exploration potential. Geol. China 33, 1181–1196 (in Chinese with English abstract).

Chen, Y.J., Ni, P., Fan, H.R., Pirajno, F., Lai, Y., Su, W.C., Zhang, H., 2007. Diagistic fluid inclusions of different types hydrothermal gold deposits. Acta Petrol. Sinica 23, 2085–2108 (in Chinese with English abstract).

Chi, G.X., Lu, H.Z., 2008. Validation and representation of fluid inclusion microthermometric data using the fluid inclusion assemblage (FIA) concept. Acta Petrol. Sinica 24, 1945–1953.

Chu, Y., Lin, W., Fayre, M., Wang, Q.C., Ji, W.B., 2012. Phanerozoic tectonothermal events of the Xuefengshan Belt, central South China: Implications from U-Pb age and Lu-Hf determinations of granites. Lithos 150, 243–255.

Clayton, R.N., O'Neil, J.R., Mayeda, T.K., 1972. Oxygen isotope exchange between quartz and water. J. Geophys. Res. 77, 3057–3067.

Collins, P.L.F., 1979. Gas hydrates in CO_2-bearing fluid inclusions and the use of freezing data for estimation of salinity. Econ. Geol. 74, 1435–1444.

Cox, S.F., Wall, V.J., Etheridge, M.A., Potter, T.F., 1991. Deformational and metamorphic processes in the formation of mesothermal vein-hosted gold

deposits—examples from the Lachlan Fold Belt in central Victoria, Australia. Ore Geol. Rev. 6, 391–423.

Dai, C.G., Chen, J.S., Lu, D.B., Ma, H.Z., Wang, X.H., 2010. Appearance and geological significance of Caledonian Movement in southeastern Guizhou, China and its adjacent area. Geol. Bull. China 29, 530–534 (in Chinese with English abstract).

Dai, C.G., Li, S., Zhang, H., 2005. Initiative discussion on tectonic evolution of southwest segment of Jiangnan Orogenic Belt: taking an example from east Guizhou and the adjacent areas. Guizhou Geol. 22, 98–102 (in Chinese with English abstract).

Dai, C.G., Zheng, Q.Q., Chen, J.S., Wang, M., Zhang, H., 2013. The metallogenic geological background of the Xuefeng-Caledonian tectonic cycle in Guizhou, China. Earth Sci. Front. 6, 219–225 (in Chinese with English abstract).

Downes, P.M.P., Seccombe, P.K., Carr, G.R., 2008. Sulfur-and lead-isotope signatures of orogenic gold mineralisation associated with the Hill End Trough, Lachlan Orogen, New South Wales, Australia. Mineral. Petrol. 94, 151–173.

Fan, H.R., Zhai, M.G., Xie, Y.H., Yang, J.H., 2003. Ore-forming fluids associated with granite-hosted gold mineralization at the Sanshandao deposit, Jiaodong gold province, China. Miner. Deposita 38, 739–750.

Fan, J.L., Luo, J.H., Cao, Y.Z., Han, W., Zhang, J.Y., 2010. Feature of geochemistry, isotope chronology and geological significance of Neoproterozoic granitic rocks in southeastern Guizhou, China. J. Northwest Univ. (Nat. Sci. Ed.) 4, 672–678 (in Chinese with English abstract).

Gao, L.Z., Dai, C.G., Liu, Y.X., Wang, M., Wang, X.H., Chen, J.S., Ding, X.Z., 2010. Zircon SHRIMP U-Pb dating of the tuffaceous bed of Xiajiang Group in Guizhou Province and its stratigraphic implication. Geol. China 37, 1071–1080 (in Chinese with English abstract).

Gao, L.Z., Chen, J.S., Dai, C.G., Ding, X.Z., Wang, X.H., Liu, Y.X., Wang, L., Zhang, H., 2014. SHRIMP zircon U-Pb dating of tuff in Fanjingshan Group and Xiajiang Group from Guizhou and Hunan Provinces and its stratigraphic implications. Geol. Bull. China 33, 949–959 (in Chinese with English abstract).

Goldfarb, R.J., Groves, D.I., 2015. Orogenic gold: Common or evolving fluid and metal sources through time. Lithos 233, 2–26.

Goldfarb, R.J., Groves, D.I., Gardoll, S., 2001. Orogenic gold and geologic time: a global synthesis. Ore Geol. Rev. 18, 1–75.

Goldstein, R.H., 2001. Fluid inclusions in sedimentary and diagenetic systems. Lithos 55, 159–193.

Hall, C.M., Kesler, S.E., Simon, G., Fortuna, J., 2000. Overlapping Cretaceous and Eocene alteration, Twin Creeks Carlin-type deposit, Nevada. Econ. Geol. 95, 1739–1752.

Hayashi, K.I., Ohmoto, H., 1991. Solubility of gold in NaCl- and H2S- bearing aqueous solutions at 250–350 °C. Geochim. Cosmochim. Acta 55, 2111–2126.

He, M.Q., Long, C.X., Wang, G.L., 2015. Origin of ore-forming fluids of Pingqiu Au ore deposit in Jinping County, southeast Guizhou Province, China. Acta Mineral. Sinica 35, 497–501 (in Chinese with English abstract).

Horne, R.J., Jodrey, M., 2001. Geology of the Dufferin gold deposit (NTS 11D/16), Halifax County. Miner. Energy Branch 1, 51–67.

Hou, G.J., Suo, S.T., Zheng, G.Z., Wei, Q.R., 1998. Caledonian orogenesis and system-transition in the Xuefengshan area. Hunan Geol. 17, 141–144 (in Chinese with English abstract).

Jäger, E., 1979. Introduction to geochronology. In: Lectures in Isotope Geology. Springer, pp. 1–12.

Jia, Y.F., Li, X., Kerrich, R., 2001. Stable isotope (O, H, S, C, and N) systematics of quartz vein systems in the turbidite-hosted Central and North Deborah gold deposits of the Bendigo cold field, Central Victoria, Australia: Constraints on the origin of ore-forming fluids. Econ. Geol. 96, 705–721.

Klein, E.L., Harris, C., Renac, C., Giret, A., Moura, C.A., Fuzikawa, K., 2006. Fluid inclusion and stable isotope (O, H, C, and S) constraints on the genesis of the Serrinha gold deposit, Gurupi Belt, northern Brazil. Miner. Deposita 41, 160–178.

Kontak, D.J., 1996. A multidisciplinary approach to detect multiple source reservoirs and processes in the formation of turbidite-hosted gold mineralisation: an example from the Meguma Terrane of Nova Scotia. In: MacDonald, D.R., Mills, K. A. (Eds.), Minerals and Energy Branch, Report of Activities 1995. Nova Scotia Department of Natural Resources Report 96–1, pp. 43.

Kontak, D.J., Smith, P.K., 1993. A metaturbidite-hosted lode gold deposit: the Beaver Dam deposit, Nova Scotia; I. vein paragenesis and mineral chemistry. Can. Mineral. 31. 471–471..

Kontak, D.J., Smith, P.K., Kerrich, R., Williams, P.F., 1990. Integrated model for Meguma Group lode gold deposits, Nova Scotia, Canada. Geology 18, 238–242.

Kontak, D.J., Horne, R.J., Kyser, K., 2011. An oxygen isotope study of two contrasting orogenic vein gold systems in the Meguma Terrane, Nova Scotia, Canada, with implications for fluid sources and genetic models. Miner. Deposita 46, 289–304.

Kretschmar, U., McBride, D., 2015. The Metallogeny of Lode Gold Deposits: A Syngenetic Perspective. Elsevier.

Kuiper, K.F., Deino, A., Hilgen, F.J., Krijgsman, W., Renne, P.R., Wijbrans, J.B., 2008. Synchronizing Rock Clocks of Earth History. Science 320, 500–504.

Li, J.W., Vasconcelos, P.M., Zhang, J., Zhou, M.F., Zhang, X.J., Yang, F.H., 2003. 40Ar/39Ar constraints on a temporal link between gold mineralization, magmatism, and continental margin transtension in the Jiaodong gold province, eastern China. J. Geol. 111, 741–751.

Li, J.W., Vasconcelos, P.M., Zhou, M.F., Zhao, X.F., Ma, C.Q., 2006. Geochronology of the Pengjiakuang and Rushan gold deposits, eastern Jiaodong gold province, northeastern China: implications for regional mineralization and geodynamic setting. Econ. Geol. 101, 1023–1038.

Li, N., Chen, Y.J., Ulrich, T., Lai, Y., 2012. Fluid inclusion study of the Wunugetu Cu–Mo deposit, Inner Mongolia, China. Miner. Deposita 47, 467–482.

Li, N., Pirajno, F., 2017. Early Mesozoic Mo mineralization in the Qinling Orogen: an overview. Ore Geol. Rev. 81, 431–450.

Lisitsin, V.A., Pitcairn, I.K., 2016. Orogenic gold mineral systems of the Western Lachlan Orogen (Victoria) and the Hodgkinson Province (Queensland): crustal metal sources and cryptic zones of regional fluid flow. Ore Geol. Rev. 76, 280–295.

Lister, G.S., Baldwin, S.L., 1996. Modelling the effect of arbitrary PTt histories on argon diffusion in minerals using the MacArgon program for the Apple Macintosh. Tectonophysics 253, 83–109.

Liu, H.B., Jin, G.S., Li, J.J., Han, J., Zhang, J.F., Zhang, J., Guo, D.Q., 2013. Determination of stable isotope composition in uranium geological samples. World Nucl. Geosci. 30, 174–179.

Liu, K., Yang, R., Chen, W., Liu, R., Tao, P., 2014. Trace element and REE geochemistry of the Zhewang gold deposit, southeastern Guizhou Province, China. Acta Geochim. 33, 109–118.

Lu, H.Z., Wang, Z.G., Wu, X.Y., Chen, W.Y., Wu, X.Y., Hu, R.Z., Keita, M., 2008. Turbidite-hosted gold deposits of SE Guizhou, China: their regional setting, mineralizing styles and some genetic constrains. In: Mao, J.W., Bierlein, F.P. (Eds.), Mineral Deposit Research: Meeting the Global Challenge: Proceedings of the Eighth Biennial SGA Meeting, Beijing, China. Springer, Berlin, pp. 545–547.

Lu, H.Z., Wang, Z.G., Wu, X.Y., Chen, W.Y., Zhu, X.Q., Guo, D.J., Keita, M., 2005. Turbidite-hosted gold deposits in SE Guizhou Province, China: their regional setting, structural control and gold mineralization. Acta Geol. Sinica 79, 98–105 (in Chinese with English abstract).

Lu, H.Z., Wang, Z.G., Chen, W.Y., Wu, X.Y., Zhu, X.Q., Hu, R.Z., 2006. Turbidite hosted gold deposits in southeast Guizhou: their structural control, mineralization characteristics, and some genetic constrains. Miner. Deposits 4, 369–387 (in Chinese with English abstract).

Luo, X.L., 1989. On the epoch of the formation of Precambrian gold deposits in Hunan province. J. Guilin College Geol. 9, 25–34 (in Chinese with English abstract).

Ma, X., Yang, K.G., Li, X.G., Dai, C.G., Zhou, Q., 2016. Neoproterozoic Jiangnan Orogeny in southeast Guizhou, South China: evidence from U-Pb ages for detrital zircons from the Sibao Group and Xiajiang Group. Can. J. Earth Sci. 53, 219–230.

McCuaig, T.C., Kerrich, R., 1998. P–T–t–deformation – fluid characteristics of lode gold deposits: evidence from alteration systematics. Ore Geol. Rev. 12, 381–453.

McDougall, I., Harrison, T.M., 1999. Geochronology and Thermochronology by the $^{40}Ar/^{39}Ar$ Method. Oxford University Press, New York.

Mernagh, T.P., Bierlein, F.P., 2008. Transport and precipitation of gold in Phanerozoic metamorphic terranes from chemical modeling of fluid-rock interaction. Econ. Geol. 103, 1613–1640.

Mikucki, E.J., Ridley, J.R., 1993. The hydrothermal fluid of Archaean lode-gold deposits at different metamorphic grades: compositional constraints from ore and wallrock alteration assemblages. Miner. Deposita 28, 469–481.

Morelli, R.M., Creaser, R.A., Selby, D., Kontak, D.J., Horne, R.J., 2005. Rhenium-Osmium geochronology of arsenopyrite in Meguma Group gold deposits, Meguma Terrane, Nova Scotia, Canada: evidence for multiple gold-mineralizing events. Econ. Geol. 100, 1229–1242.

Neall, F.B., Phillips, G.N., 1987. Fluid-wall rock interaction in an Archean hydrothermal gold deposit; a thermodynamic model for the Hunt Mine, Kambalda. Econ. Geol. 82, 1679–1694.

Ni, P., Wang, G.G., Chen, H., Xu, Y.F., Guan, S.J., Pan, J.Y., Li, L., 2015. An Early Paleozoic orogenic gold belt along the Jiang–Shao Fault, South China: evidence from fluid inclusions and Rb–Sr dating of quartz in the Huangshan and Pingshui deposits. J. Asian Earth Sci. 103, 87–102.

No.6 team of Non-ferrous Metals and Nuclear Industry Geological Exploration Bureau of Guizhou, 2002. Geological report of the Pingqiu gold mine region in Jinping country, Guizhou province. pp. 1–11 (in Chinese).

Peng, J.T., Dai, T.G., 1998. On the mineralization epoch of the Xuefeng gold metallogenic province. Geol. Prospect. 34, 37–41 (in Chinese with English abstract).

Peng, J.T., Dai, T.G., Hu, R.Z., 2000. Geochemical evidence for the ore-forming materials of gold deposits, southwestern Hunan. Acta Mineral. Sinica 19, 327–334 (in Chinese with English abstract).

Peng, J.T., Hu, R., Zhao, J., Fu, Y., Lin, Y., 2003. Scheelite Sm-Nd dating and quartz Ar-Ar dating for Woxi Au-Sb-W deposit, western Hunan. Chin. Sci. Bull. 48, 2640–2646.

Phillips, D., Fu, B., Wilson, C.J., Kendrick, M.A., Fairmaid, A.M., Miller, J.M., 2012. Timing of gold mineralisation in the western Lachlan Orogen, SE Australia: a critical overview. Aust. J. Earth Sci. 59, 495–525.

Phillips, G.N., Powell, R., 2010. Formation of gold deposits: a metamorphic devolatilization model. J. Metamorph. Geol. 28, 689–718.

Qin, Y.J., Du, Y.S., Mu, J., Lu, D.B., Long, J.X., Wang, A.H., Zhang, H.S., Zeng, C.X., 2015. Geochronology of Neoproterozoic Xiajiang Group in Southeast Guizhou, South China, and its geological implications. Earth Sci. J. China Univ. Geosci. 40, 1107–1120 (in Chinese with English abstract).

Ramboz, C., Pichavant, M., Weisbrod, A., 1982. Fluid immiscibility in natural processes: Use and misuse of fluid inclusion data: II. Interpretation of fluid inclusion data in terms of immiscibility. Chem. Geol. 37, 29–48.

Ramsay, W.R.H., Bierlein, F.P., Arne, D.C., 1998. Turbidite-hosted gold deposits of Central Victoria, Australia: their regional setting, mineralising styles, and some genetic constraints. Ore Geol. Rev. 13, 131–151.

Ran, R.D., Li, P., 2007. Analysis of gold deposit types and exploration potential of the southeastern Guizhou gold district. In: The Second Creative Development Forum of Gold Industry in Western China, pp. 35–39 (in Chinese).

Ridley, J.R., Diamond, L.W., 2000. Fluid chemistry of orogenic lode gold deposits and implications for genetic models. Rev. Econ. Geol. 13, 141–162.

Ryan, R.J., Smith, P.K., 1998. A review of the mesothermal gold deposits of the Meguma Group, Nova Scotia, Canada. Ore Geol. Rev. 13, 153–183.

Sangster, A.L., Smith, P.K., 2007. Metallogenic summary of the Meguma gold deposits, Nova Scotia. Mineral Deposits of Canada: A Synthesis of Major Deposit-Types, District Metallogeny, the Evolution of Geological Provinces, and Exploration Methods: Geological Association of Canada, Mineral Deposits Division, Special Publication 5, 723–732.

Shi, M.K., Fu, B.Q., Jin, X.X., Zhou, D.Z., 1993. Antimony Deposits in Central Hunan Province. Hunan Science and Technology Press, Changsha, pp. 41–52 (in Chinese).

Song, B.C., 2014. Distribution characteristics and ore-forming regularities of turbidite-hosted gold deposits in Hunan, Yunnan and Guangxi. Gold 6, 26–32.

Steele-MacInnis, M., Lecumberri-Scanchez, P., Bodnar, R.J., 2012. HokieFlincs_H_2O-NaCl: a microsoft excel spreadsheet for interpreting PVTX properties of H_2O-NaCl. Comput. Geosci. 49, 334–337.

Steiger, R.H., Jäger, W., 1977. Subcommission on geochronology: convention on the use of decay constants in geo-and cosmochronology. Earth Planet. Sci. Lett. 36, 359–362.

Tang, S.K., Ma, X., Yang, K.G., Deng, X., Dai, C.G., Zhang, H., Zhou, Q., 2014. Characteristics and genesis of two types of tectonic deformation during Caledonian in eastern Guizhou and Northern Guangxi. Geoscience 28, 109–118 (in Chinese with English abstract).

Tao, P., Chen, Q.F., Wang, L., Hu, C.L., 2013. Location prediction of gold deposits for ore field grade in the Tianzhu-Jinping-Liping area, southeastern Guizhou, China: the method on potential assessment of mineral resources of low-exploration and study degree area. J. Jilin Univ. (Earth Sci. Ed.) 4, 1235–1245 (in Chinese with English abstract).

Tao, P., Xiao, X.D., Zhang, H., 2009. The Au-bearing sedimentary sequences and their impact on the gold deposits in light metamorphic rock in the boundary of Hunan, Guizhou and Guangxi regions. Geol. Sci. Technol. Inf. 2, 110–114 (in Chinese with English abstract).

Tao, P., Yao, S.Z., Wang, L., Wang, C.W., 2012. Metallogenic unit division and its ore-control factors of gold deposit in Tianzhu-Jinping-Liping area of southeast Guizhou. Guizhou Geol. 4, 241–248 (in Chinese with English abstract).

Taylor, H.P., 1997. Oxygen and hydrogen isotope relationships in hydrothermal mineral deposits. In: Barnes, H.L. (Ed.), Geochemistry of Hydrothermal Ore Deposits. Wiley and Sons, New York, pp. 229–302.

Tomkins, A.G., 2013. On the source of orogenic gold. Geology 41, 1255–1256.

Wang, J.S., Wen, H.J., Li, C., Ding, W., Zhang, J.R., 2011. Re-Os isotope dating of arsenopyrite from the quartz vein-type gold deposit, southeastern Guizhou province, and its geological implications. Acta Geol. Sinica 85, 955–964 (in Chinese with English abstract).

Wang, J.S., Zhou, J.X., Yang, D.Z., Liu, J.H., 2012. Geochemistry and zircon U-Pb age of the Zaibian Diabase, SE Guizhou Province, SW China. Acta Geol. Sinica 86, 460–469 (in Chinese with English abstract).

Wang, L., Tao, P., 2012. Application of 1/200,000 regional gravity and magnetic data to infer concealed rock mass in east of Guizhou. Comput. Tech. Geophys. Geochem. Explor. 34, 449–454 (in Chinese with English abstract).

Wang, S.Y., Zhang, L.X., Tao, P., Dai, C.G., 2006. Geological characteristics and mineralization of quartz-vein-type gold deposits in east of Guizhou. Guizhou Geol. 1, 36–43 (in Chinese with English abstract).

Wang, X.L., Zhou, J.C., Griffin, W.L., Zhao, G.C., Yu, J.H., Qiu, J.S., Zhang, Y.J., Xing, G.F., 2014. Geochemical zonation across a Neoproterozoic orogenic belt: isotopic evidence from granitoids and metasedimentary rocks of the Jiangnan orogen, China. Precambr. Res. 242, 154–171.

Wang, X.Z., Liang, H.Y., 2000. Wang Xiuzhang, Liang Huaying, Cheng Jingping. Main characteristics of Caledonian gold deposits in South China. Miner. Deposits 19, 1–8 (in Chinese with English abstract).

Wang, X.Z., Liang, H.Y., Shan, Q., Chen, J.P., Xia, P., 1999. Metallogenic age of the Jinshan gold deposit and Caledonian gold mineralization in South China. Geol. Rev. 45, 19–25 (in Chinese with English abstract).

Willman, C.E., Wilkinson, H.E., 1992. Bendigo goldfield: Spring Gully, Golden Square, Eaglehawk: Department of Primary Industries, Minerals and Petroleum Division, East Melbourne, Victoria, Australia Geological Survey Report (Victoria) 93.

Wilson, C.J.L., Schaubs, P.M., Leader, L.D., 2013. Mineral precipitation in the quartz reefs of the Bendigo gold deposit, Victoria, Australia. Econ. Geol. 108, 259–278.

Wu, S.C., 2013. The Yearbook of Qiandongnan Autonomous Prefecture, Guizhou province, China. The Kaiming Press, Beijing (in Chinese).

Wu, S.C., 2014. The Yearbook of Qiandongnan Autonomous Prefecture, Guizhou province, China. The Kaiming Press, Beijing (in Chinese).

Wu, S.C., 2015. The Yearbook of Qiandongnan Autonomous Prefecture, Guizhou province, China. The Kaiming Press, Beijing (in Chinese).

Wu, W.M., Liu, J.Z., Wang, Z.P., Yu, D.L., 2015. Indicative significance of H-O isotope and fluid inclusion in ore-forming fluid of Pingqiu gold mine, Guizhou province. Gold Sci. Technol. 23, 30–36 (in Chinese with English abstract).

Yoo, B.C., Lee, H.K., White, N.C., 2010. Mineralogical, fluid inclusion, and stable isotope constraints on mechanisms of ore deposition at the Samgwang mine (Republic of Korea)—a mesothermal, vein-hosted gold–silver deposit. Miner. Deposita 45, 161–187.

Yu, D.L., 1997. A study on ore-hunting indicators for endogenetic gold deposits in eastern Guizhou. Guizhou Geol. 1, 55–63 (in Chinese with English abstract).

Zeng, W., Zhou, H.W., Zhong, Z.Q., Zeng, Z.G., Li, H.M., 2005. Single zircon U-Pb ages and their tectonic implications of Neoproterozoic magmatic rocks in southeastern Guizhou, China. Geochemica 6, 10–18 (in Chinese with English abstract).

Zhang, J., 2001. Geochemistry of fluid inclusions from the Moshan-Youma'ao gold deposit, Tianzhu, eastern Guizhou. Acta Mineral. Sinica 21, 102–106 (in Chinese with English abstract).

Zhu, H.P., Wang, L.J., 2002. Determining gaseous composition of fluid inclusions with Quadrupole Mass Spectrometer. Sci. China, Ser. D Earth Sci. 45, 97–102.

Zhu, X.Q., Wang, G.L., Lu, H.Z., Wu, X.Y., Chen, W.Y., 2006. Determination of the age of gold deposits in southeastern Guizhou: with a discussion of the Caledonian Hunan-Guizhou gold ore belt. Geol. China 5, 1092–1099 (in Chinese with English abstract).

Zhu, Y.F., An, F., Tan, J., 2011. Geochemistry of hydrothermal gold deposits: a review. Geosci. Front. 2, 367–374.

Zhu, Y.T., 1992. The relationship between the hydrothermal metal ores and the ring structures in southeastern Guizhou. Guizhou Geol. 9, 63–71 (in Chinese with English abstract).